FACULDADE DE ENGENHARIA DA UNIVERSIDADE DO PORTO

Network Connectivity Inference in Neuronal Cultures from Multi-Electrode Recordings: Towards a Real-Time Implementation

Ana Beatriz de Matos Barros

Mestrado em Bioengenharia – Engenharia Biomédica

Supervisor: Dr. Paulo Aguiar

September 22, 2023

Resumo

O cérebro humano é uma das mais fascinantes, ainda que em grande parte inexplorada, estruturas no universo. A sua notável complexidade estrutural e funcional é o resultado de um longo processo evolutivo quer a nível celular quer ao nível da organização dos circuitos neuronais. O estabelecimento do sistema nervoso – e, em particular, do cérebro humano – requer uma coordenação rigorosa de uma série de eventos moleculares e celulares nas diferentes fases do desenvolvimento neuronal. A formação de redes intrincadamente organizadas de ligações sinápticas entre diversos tipos de neurónios é um passo fundamental neste processo. Estes agrupamentos de neurónios são cruciais para a representação de informação no sistema nervoso, e a sua crescente complexidade traduz-se em extraordinárias capacidades computacionais que sustentam funções cerebrais superiores: perceção, cognição, emoção e ação. Desvendar a conectividade dos circuitos neuronais fornece informações preciosas sobre os mecanismos que suportam estes processos neurofisiológicos. Técnicas avançadas de neuroimagem e ferramentas de eletrofisiologia têm possibilitado grandes avanços neste campo. Com este trabalho, visa-se o desenvolvimento de um novo método de inferência de conectividade neuronal em tempo real. Um novo algoritmo de análise computacional baseado em métricas de correlação permite continuamente inferir e atualizar as ligações entre elementos neuronais a partir de sinais eletrofisiológicos à medida que estes vão sendo obtidos. Esta inferência de conectividade neuronal em tempo real tem elevada utilidade em dois contextos complementares: i) em investigação fundamental, onde as manipulações experimentais (*e.g.*, farmacológicas ou elétricas) a uma população neuronal passam a poder ter em consideração a conectividade da rede; e ii) em contexto clínico, onde potenciais sistemas de neuromodulação com multi-elétrodos podem usar informação atualizada da conectividade da rede para desenvolver e adaptar protocolos de estimulação elétrica. O algoritmo foi validado com dados sintéticos de modelos neuronais computacionais, e posteriormente testado com dados experimentais reais de circuitos neuronais *in vitro* com diferentes configurações. Os resultados são apresentados em representações visuais informativas e intuitivas a partir de implementações computacionais especificamente desenvolvidas para este efeito. Esta dissertação tem o potencial de aprimorar a compreensão de circuitos neuronais, e abre novas oportunidades para abordagens baseadas na informação de conectividade em neurociência.

Palavras-chave: análise em tempo real, atividade eletrofisiológica, conectividade, correlação, matrizes de microeléctrodos, modelos computacionais neuronais, redes neuronais biológicas.

Abstract

The human brain is one of the most fascinating, yet still largely unexplored, structures in the known universe. Its remarkable structural and functional complexity is the product of a long evolutionary process at both the cellular and network levels. The precise wiring of the nervous system – and, in particular, of the human brain – requires a tight coordination of a series of molecular and cellular events at the different stages of neural development. The formation of intricately organized networks of synaptic connections among diverse neuronal types is a fundamental step in this process. These neuronal assemblies are crucial for the representation of information in the nervous system, and their increasing complexity translated into extraordinary computational capabilities that support higher brain functions: perception, cognition, emotion and action. Unravelling the connectivity of neuronal circuits provides valuable insights into the mechanisms behind these neurophysiological processes. New high-throughput methods, including advanced neuroimaging techniques and electrophysiology tools, have enabled significant advances in this field. This work aims at developing a new method for real-time inference of neuronal connectivity. A novel computational analysis algorithm based on correlation metrics allows for the continuous inference and update of connections among neuronal elements from electrophysiological signals as they are acquired. Such real-time inference of neuronal connectivity has a relevant role in two complementary contexts: i) in fundamental research, where experimental manipulations (*e.g.*, pharmacological or electrical) on neuronal populations can take into account the network connectivity; ii) in clinical context, where potential multi-electrode neuromodulation systems can use real-time feedback from network connectivity to tailor electrical stimulation protocols. The algorithm was validated with synthetic data from computational neuronal models, and further tested with real experimental data from *in vitro* engineered controlled neuronal circuits. Results are presented in informative and intuitive visual representations using computational implementations specifically developed for this purpose. This dissertation has the potential to enhance our understanding of neuronal circuits and opens new opportunities for connectivity-informed approaches in neuroscience.

Keywords: biological neuronal networks, computational neuronal modelling, connectivity, correlation, electrophysiological activity, microelectrode arrays, real-time analysis.

Agradecimentos

Ao meu orientador, o Dr. Paulo Aguiar, a quem serei para sempre grata pela oportunidade de pensar, questionar e fazer neurociência num grupo de investigação tão entusiasta e inspirador como o NCN. Obrigada por me encorajares a sair da minha zona de conforto, mesmo quando dá "borboletas na barriga", pelos sábios conselhos nas horas mais cinzentas, e por tudo o que aprendi e, com certeza, continuarei a aprender contigo. A cada um dos NCNers, obrigada por me terem feito sentir parte de uma verdadeira equipa desde o primeiro dia. Esta dissertação tem, seguramente, um bocadinho de cada um de vocês. Como prometido – e, mais importante ainda, como merecido –, obrigada Miguel não só por arriscares as tuas culturas, mas, sobretudo, pela sempre pronta ajuda. Aos meus companheiros e amigos de Mestrado, com quem tive a sorte de partilhar o bom e o menos bom dos últimos meses, obrigada pelas conversas sinceras, pelos desabafos, e por terem estado por perto sempre que o ânimo escasseava.

Aos meus pais, por acreditarem mais em mim do que, por vezes, eu acredito em mim mesma, e para quem vou querer sempre voltar. Obrigada por me relembrarem que "amanhã também é dia" de cada vez que eu acho que o mundo vai acabar. Sem o vosso apoio inabalável, dificilmente teria chegado aqui. Ao meu irmão, por conseguir sempre me fazer rir. A toda a minha família, por serem casa sempre que preciso.

Aos meus amigos, àqueles com quem, em tempos, brinquei no recreio da escola, e àqueles que que se tornaram no melhor que a faculdade me deu, obrigada por terem sempre as palavras certas, pelas aventuras que nunca pensei viver, e por me mostrarem que há muito mais na vida para além do que eu achava que me estava destinado.

“Go as far as you can see; when you get there, you’ll be able to see farther.”

J. P. Morgan

Contents

List of Figures

List of Tables

Abbreviations

CC	Cross-Correlation
CCH	Cross-Correlation Histogram
cISI	Cross-Interspike Intervals
CMD	Compartmentalized Microfluidic Device
CMOS	Complementary Metal-Oxide Semiconductor
DBS	Deep Brain Stimulation
DLL	Dynamic Link Library
DSP	Digital Signal Processor
DTE	Delayed Transfer Entropy
FNCCH	Filtered and Normalized Cross-Correlation Histogram
GUI	Graphical User Interface
HD-MEA	High-Density Micro-Electrode Array
HH	Hodgkin-Huxley
HOTE	High Order Transfer Entropy
IFB	Interface Board
JE	Joint Entropy
MCS	MultiChannel Systems
MD	Movement Disorder
MEA	Micro-Electrode Array
MI	Mutual Information
MRI	Magnetic Resonance Imaging
NMODL	NEURON MODeling Language
PC	Partial Correlation
PDL	Poly-D-Lysine
PDMS	Polydimethylsiloxane
PHN	Primary Hippocampal Neurons
RMSE	Root Mean Square Error
SWM	Synaptic Weight Matrix
TE	Transfer Entropy

USB	Universal Serial Bus
μEF	microElectrode Arrays and microFluidics devices

Chapter I

Introduction

Neurons are traditionally regarded as the structural and physiological units of the nervous system. The neuron doctrine was first introduced by Santiago Ramón y Cajal in 1891, and it established the fundamental principles supporting modern neuroscience research for over a century [1].

The intrinsic morphological and electrophysiological properties of neuronal cells are essential for their assembly into diverse functional neuronal circuits during neural development. However, recent advances in multineuronal recording techniques have revealed that neuronal dynamics – and ultimately brain-wide activity – mostly reflect complex direct and indirect interactions among neuronal and non-neuronal cells [2], [3]. Several studies have investigated putative structure-function relationships in biological neuronal networks, both *in vitro* and *in vivo* [4], [5]. Accordingly, a novel paradigm for neuroscience research suggests that hierarchically organized neuronal assemblies form physiological units that support the basic neuronal computations underlying higher-level brain function, and the complex neuronal dynamics emerging from these neuronal populations are strongly shaped by the patterns of local connectivity, known as network motifs [6], [7].

The characterization of the structure-function relationship remains a long-standing challenge in the field of complex dynamic systems, of which the brain is an example *par excellence* [8]. Current research focuses on understanding how brain function arises from neuronal interactions at multiple temporal and spatial scales. Neural mechanisms of learning and memory rely on complex neuronal network phenomena, including the formation of new connections and the alteration and/or elimination of pre-existing connections [9]. Moreover, aging-related processes and neurodegenerative diseases have been reportedly associated with profound alterations in structural and functional brain networks [10], [11]. Brain network measures may help elucidate the pathophysiological mechanisms of brain dysconnectivity [12], and derive clinically relevant

connectivity-based biomarkers for the diagnosis, monitoring and treatment of neurodegenerative diseases and other neurological disorders [13].

1.1 Motivation

The connectome is defined as "a comprehensive structural description of the network of elements and connections" in the nervous system [14]. Connectomic studies employ advanced neuroimaging and electrophysiological techniques to reconstruct neuronal circuits across multiple spatial scales [15]. Computationally informed approaches based on the neuronal wiring diagram may prove valuable in addressing neuroscience questions that either aim at targeting specific functionally relevant network motifs, or at precisely manipulating and/or controlling connectivity patterns in neuronal assemblies [16].

In fundamental neuroscience research, the *in vitro* study of neuronal dynamics routinely involves temporal and/or spatial manipulations (*e.g.*, pharmacological studies) that often rests on (unconfirmed) assumptions on how the neurons may be connected. This limitation also extends to neuromodulation protocols, which would require a preliminary study on the neuronal network dynamics to determine optimal stimulation locations and parameters [17]. Neuronal circuits are manually probed before each experiment to identify target sites that are capable of triggering a consistent response in the surrounding network upon minimal stimulation; however, this can be a time-consuming trial-and-error process. Connectivity maps derived from neural recording data may reveal distinct topological network features that are critically important for the global function of neuronal circuits. Densely connected hub neurons are thought to play a central role in information integration due to their high degree of connectivity to other network regions [18]. Single-hub neuron perturbations profoundly impact network-wide dynamics, and thus these network elements constitute attractive target candidates for neuromodulation [19]. Moreover, neural plasticity phenomena occurring over a range of time scales can significantly affect the neuronal network dynamics, and thereby require adaptations to the stimulation protocol in response to changes in the underlying network topology.

In clinical neuroscience research, a new generation of implantable neurostimulation devices with neural recording capabilities is opening new avenues towards adaptive closed-loop therapies for neurological disorders [20]. Deep brain stimulation (DBS) is an established symptomatic treatment for common movement disorders (MD), such as Parkinson's disease and essential tremor, and other neuropsychiatric conditions. Conventional DBS (cDBS) technologies deliver continuous fixed-parameter electrical stimulation to target brain structures regardless of the ongoing neuronal activity [21]. Although the precise physiological mechanisms underlying the effectiveness of DBS remain poorly understood, the "disruption hypothesis" suggests that

electrical stimulation interrupts pathological information flow between connected brain regions, producing similar therapeutic effects to neurosurgical lesioning [22]. Adaptive deep brain stimulation (aDBS) is emerging as a promising neuromodulation therapy for designing data-driven stimulation protocols using real-time feedback from physiological measures linked to pathological states – biomarkers [23]. Besides providing insight into the pathological features of neurological disorders and the therapeutic mechanisms of action of DBS, patient-specific connectivity profiles of local microcircuits may serve as effective biomarkers to guide neuromodulation therapies and, ultimately, improve short- and long-term clinical outcomes [16].

Thus far, developed neuronal connectivity inference algorithms have focused on offline estimation, *i.e*, after the data acquisition is completed. However, the above-mentioned scenarios would benefit from an online implementation that enables monitoring network topology in real-time, continuously updating the estimates as new data arrives. Indeed, inferring neuronal connectivity in real-time has the potential to drive fundamental and translational research studies in the field of neuroscience.

1.2 Challenges

Reconstructing neuronal circuitry is not a straightforward task. Correlation-based metrics and information theory concepts are extensively used to characterize connectivity in biological neuronal networks [24], but a detailed description of the neuronal wiring diagram at cellular resolution is still lacking in most of the approaches. Also, different methods are based on different concepts, and its interpretation and comparison are therefore challenging.

The high dimensionality of neural recordings is a major problem in the analysis of such data. Although new electrode technologies provide distinctive information on the nature of neuronal circuits with an unprecedented spatiotemporal resolution, computational analysis methods struggle with efficiently keeping up with these advances as the number of electrodes/neurons grows. This problem is particularly relevant when considering an online implementation, in which the results of the analyses have to be provided in real-time.

1.3 Objectives and contributions

The main goal of this dissertation is to implement novel and robust computational analysis methods for inferring connectivity in biological neuronal networks from electrophysiological activity (spiking activity) in real-time. The presented framework aims at detecting and further characterizing interactions between neuronal elements in terms of their

connection strength, direction, latency, and type (excitatory or inhibitory), and particularly at deriving detailed neuronal wiring diagrams in real-time. In addition, informative and intuitive visual representations of connectivity data are proposed herein. This work makes extensive use of i) computer simulations of biophysically detailed neuronal models where connectivity is fully known, and ii) high spatiotemporal resolution electrophysiology recordings using microelectrode arrays from *in vitro* neuronal populations with constrained connectivity. Both contexts are used to develop, validate and test the proposed methods.

1.4 Document structure

This document is organized into six chapters. Chapter I introduces the topic of this dissertation and outlines the main objectives and challenges of the present work. Chapter II provides a brief overview of the fundamental properties of neurons, including the neuronal mechanisms underlying signal generation and transmission in the nervous system and the state-of-the-art tools for probing neuronal circuits. Chapter III reviews current computational analysis methods for inferring connectivity in biological neuronal networks from neural activity recordings. The strengths and limitations of each method are presented. Chapter IV details on the materials and methodologies implemented in this work, namely how neuronal data was obtained, and the computational tools used for the subsequent analysis. Chapter V presents the main findings of this work and discusses their implications. A novel approach to infer connectivity in real-time is proposed and its strengths and limitations are discussed. Results on synthetic data for validation are presented, followed by tests on experimental data featuring different network configurations. Finally, Chapter VI outlines the main conclusions of this work and suggests future research directions.

Chapter II

Core concepts on neurobiology

In this chapter, an overview is provided on the structural and functional role of neurons in the nervous system. The fundamental mechanisms of neuronal information processing and transmission are briefly described, and the contribution of novel electrode technologies to further advance our understanding of brain function is discussed.

2.1 Neuroanatomy

Historically, the role of neurons in the nervous system has been a matter of debate in the scientific community. Early studies on brain organization described the nervous system as a single continuous network – the reticulum [25]. In 1887, Santiago Ramón y Cajal started investigating the nervous system using a new staining technique for nervous fibres ("the black reaction") [25]. Based on his observations, Ramón y Cajal argued that the nervous system consisted of discrete cellular units and proposed a different viewpoint – the neuron doctrine [1].

A typical neuron consists of three main compartments: cell body, dendrites, and axon. The cell body, also known as soma, contains the nucleus and coordinates the cell's activities. Dendritic and axonal processes both extend from the soma. Electrochemical signals from nearby neurons are integrated in the dendrites, which form intricately branched structures in the vicinity of the soma – the dendritic tree. The axon transmits these signals to other target cells and, can vary substantially in length, ranging from a few millimeters to several meters [26]. The neuronal polarity emerges from the asymmetrical distribution of structurally and functionally distinct sub-cellular structures: dendrites and axon. These specialized structures establish the direction in which neuronal information propagates, from dendrites towards the axon terminals [27]. By imposing unidirectionality, information can be reliable conveyed along defined pathways in the nervous system.

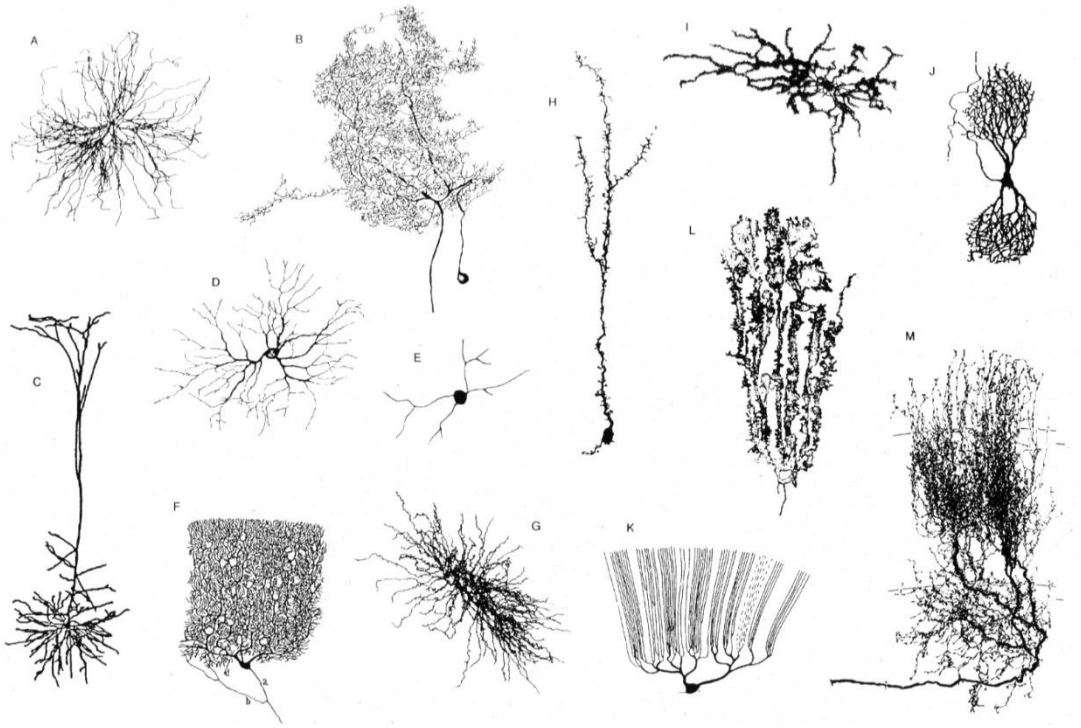

Figure II-1. Cellular diversity in the hippocampus. The morphological diversity of neuronal cells reflects the complexity of brain function [24].

Although common traits are found across different neuronal types, the most simplistic representations are unable to capture the morphological diversity displayed by these cells (**Figure II-1**) [28]. In addition, physiological, molecular and connectivity-based properties provide relevant distinguishing features for cell-type classification [29]. The hippocampus is a classic example of cellular diversity, with more than twenty different types of inhibitory interneurons described [30]. This remarkable heterogeneity reflects the functional diversity required to regulate and control cognitive processing in the hippocampus and suggests a close interplay between cellular and functional diversity in other neuronal circuits.

A fundamental property of neurons is their ability to communicate with other cells. The transmission of information between neurons primarily takes place in specialized structures called synapses. Synapses are usually established between the axon terminals of a pre-synaptic neuron and the dendritic processes of a post-synaptic neuron. Depending on the evoked post-synaptic response, synapses can be classified as excitatory or inhibitory, whether the membrane is locally depolarized or hyperpolarized, respectively. Chemical synapses involve the release of neurotransmitters at the synaptic gap and are the more commonly found in the nervous system, although electrical synapses based on gap junctions can also be found [31]. These connections are not immutable over time. Neuroplasticity phenomena are involved in neuronal processes such as learning and memory formation, where the strength of synapses can be tuned to modify the relevance of a given connection in the circuit [32].

For several decades, neurons have been the main object of study in neuroscience. However, other non-neuronal cells are found in the nervous system, known as the glial cells. Glia, from the Greek word "*glía*" meaning glue, are, as the name suggests, key elements for supporting the neuronal function and maintaining the integrity of the nervous system [33].

2.2 The neuronal membrane

Biological membranes are primarily composed of a double layer of phospholipids. This physical barrier allows to establish an asymmetric distribution of charge between the inside and outside of the cell. The charge imbalance generates a difference in electrical potential across the membrane, known as the membrane potential, V_m [34]. The membrane potential can be measured by placing an electrode into a cell and using the extracellular medium as the reference for a second electrode, with $V_m = V_{in} - V_{out}$.

Membrane proteins embedded in the lipidic bilayer are involved in multiple cellular processes. Transmembrane channel proteins mediate the passage of ions and other molecules across the membrane. The mechanisms underlying their function are very diverse, but essentially two types of channels can be distinguished: non-gated and gated channels. Non-gated channels, also known as leakage channels, have an approximately constant conductance. In contrast, gated channels undergo conformational changes in response to different signals, switching between an open and a closed state. Voltage-gated channels conduct ions according to changes in the membrane potential and are particularly relevant to signal transmission in neurons. Moreover, ions channels may exhibit selectivity to distinct ion species, mainly based on their size and charge [35].

The movement of ions through the membrane channels is determined by the electrochemical gradient for each specific ion. The electrochemical gradient arises from the combined effects of a concentration gradient and an electrical gradient. When the concentration of a given particle is higher in one region than in another, a concentration gradient is created. The particles will naturally move down the concentration gradient, from areas with higher concentrations to areas with lower concentrations, through a process called diffusion. On the other hand, an electrical gradient occurs when there is an unequal distribution of charges between two regions. In this case, ions will drift towards regions with lower potential energy. The membrane potential at which the diffusion current for a given ion X is balanced by the electrical drift, with no net current across the membrane, is the equilibrium potential for the ion, E_X, also known as its reversal potential [36].

The Nernst equation is used to compute the reversal potential of an ion X considering the concentration, $[X]$, on both sides of the membrane,

$$E_X = \frac{RT}{zF} \ln \frac{[X]_{out}}{[X]_{in}} \quad [1]$$

where R stands for the gas constant, T is the temperature, in K, F corresponds to the Faraday's constant, and z is valence of the ion ($z = +1$ for both sodium and potassium) [36].

Sodium and potassium ions are key charge carriers to signal generation and propagation in neurons. At rest, sodium ions are at a relatively higher concentration outside the cells, while a higher concentration of potassium ions is found within the cells. Thus, sodium tends to move into the cells, driving the membrane potential towards its equilibrium potential, $E_{Na} = +50mV$, and potassium tends to diffuse out of the cells, until its equilibrium potential, $E_K = -70mV$ is reached. The differences in concentration across the membrane for these ions are maintained by Na^+/K^+ pumps. These active transporters use ATP to move ions against their concentration gradient, exchanging 3 intracellular sodium ions for 2 extracellular potassium ions. Different ions contribute to the resting membrane potential, E_m, which typically is around $-70\ mV$. This value is closer to the potassium equilibrium potential since, at rest, the permeability of potassium channels is significantly larger than for other channels [36].

Considering an infinitesimal patch of membrane, two parallel effects can be distinguished: the membrane capacitance, C_m, and the membrane resistance, R_m. Biological membranes act as electrical insulators, enabling the separation of charges on both sides of the membrane. This property can be described by a capacitor, with a capacitance $C_m = Q/V_m$, where Q is the accumulated charge and V_m is the membrane potential. The resistance of the membrane to the flow of an ion X can be modelled as a constant resistance, R_X, in series with a voltage source equal to the corresponding equilibrium potential, E_X. For a given ion, when the current across the membrane is zero, the membrane potential equals the equilibrium potential of the ion. The equivalent membrane resistance, R_m, accounts for the individual contributions of each ion. The passive properties of neuronal membranes can be represented by the simplified electric circuit in F, where E_m corresponds to the resting membrane potential [36].

The passive membrane model is a simple resistor-capacitor (RC) circuit (**Figure II-2**). The current across the membrane, I_m, is given by the sum of currents through the resistor and into the capacitor, $I_m = I_R + I_C$. At rest, $I_m = 0$. When a perturbation is introduced, for instance, in the form of an injected current, I_{inj},

$$I_{inj} = I_R + I_C \quad [2]$$

Based on the current-voltage relation for a resistor and a capacitor,

$$I_{inj}(t) = \frac{1}{R_m}(V_m(t) - E_m) + C_m \frac{dV_m(t)}{dt} \quad [3]$$

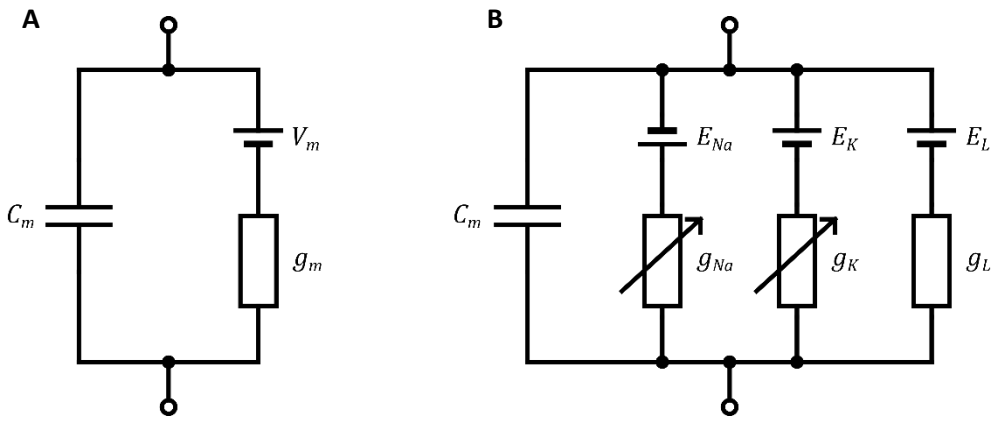

Figure II-2. Equivalent circuits for a patch of neuronal membrane. On the left, the passive properties of the neuronal membrane are represented. On the right, the equivalent circuit considering the active properties of the membrane is shown.

Solving the first order differential equation for a constant current I_{inj},

$$V_m(t) = V_\infty + (V_\infty - V_0)e^{-\frac{t}{\tau_m}} \quad [4]$$

where V_∞ is given by $V_\infty = E_m + R_m I_{inj}$, V_0 is the initial membrane potential, and τ_m is the membrane time constant, expressed as $\tau_m = R_m C_m$. From **Equation 4**, the membrane potential, V_m, decays to a new value, V_∞, as a function of the injected current with a time constant equal to τ_m.

The circuit model in **Figure II-2** can be extended to consider the spatial component for the propagation of perturbations along the membrane. Individual circuits corresponding to membrane patches can be combined in series to derive the cable equation and model the membrane potential in time and space. Besides the membrane time constant, this representation also includes a space constant, relating the attenuation of the signal with the distance to the origin of the perturbation.

Passive properties are insufficient to support effective signal propagation along neurons [36]. In 1952, Hodgkin and Huxley proposed a mathematical model to describe the mechanisms underlying signal generation and transmission in the giant squid axon [37]. The squid axon represented a suitable model system to study these mechanisms given its unusually large diameter, facilitating its manipulation during electrophysiological experiments. Although the model was derived from the dynamics exhibited by the squid giant axon, it provided the foundations for subsequent studies with other animal models.

The Hodgkin-Huxley (HH) model relies on the activity of voltage-gated channels. These protein complexes alter their conformation in response to local changes in the membrane potential, affecting the membrane permeability to different ion species. In their experiments, Hodgkin and

Huxley elucidated the role of voltage-gated channels by clamping the membrane potential at various levels and isolating the dynamics of sodium and potassium ions [37].

Voltage-gated channels are characterized by two fundamental states: an open state, in which their permeability is increased, and a closed state, in which the passage of ions is significantly reduced. The transitions between these two states can be described by the rate coefficients α and β, where α is the rate constant determining the transition from the closed to the open state, and β corresponds to the opposite transition. These coefficients are voltage-dependent and allow to express the fraction of open channels, x, as a function of the membrane potential and time.

$$\frac{dx}{dt} = \alpha_X(V) \cdot (1 - x) - \beta_X(V) \cdot x, \qquad X = m, n, h \tag{5}$$

where m and n are the activation variables for sodium and potassium ions, respectively. Besides activation, in which ion channels are activated when the membrane potential increases significantly, sodium channels are governed by a second gating variable, h. This variable describes the inactivation of sodium channels following the membrane depolarization, with an opposite effect to the one related with the gating variable m [36].

Considering the gating variables, the conductance, g, for a specific ion can be expressed by combining the conductance of all the respective open channels,

$$g_{Na} = \overline{g}_{Na} m^3 h \tag{6}$$

$$g_K = \overline{g}_K n^4 \tag{7}$$

where $\overline{g}_{Na}$ and $\overline{g}_K$ are the maximum conductance for sodium and potassium channels, respectively. The exponents were derived by fitting the model to the experimental data. Later studies revealed how these values were in fact related to the number of subunits that compose each ion channel [36].

The ionic current, I_X, for a given ion can be calculated as

$$I_X = g_X(V_m - E_X) \tag{8}$$

where the difference between the membrane potential and the equilibrium potential of X corresponds to the so-called driving force. When these two quantities are equal, the net current across the membrane is zero. The contributions of the sodium and potassium currents, along with the membrane capacitive component and a constant leakage conductance, allow to describe the membrane current, I_{inj}, as a function of the membrane voltage, V_m, and time.

$$I_{inj} = \overline{g}_{Na} m^3 h(V_m - E_{Na}) + \overline{g}_K n^4 (V_m - E_K) + \overline{g}_L (V_m - E_L) + C_m \frac{dV_m}{dt} \tag{9}$$

The equivalent circuit is represented in **Figure II-2**.

This mathematical model provides a detailed description of the temporal sequence of events involved in the initiation and propagation of action potentials. When the membrane potential exceeds a certain voltage, sodium channels are activated, and sodium ions flow into the cell. As more sodium ions cross the membrane, the membrane potential is driven towards its reversal potential. The delayed activation of potassium channels causes a decrease in the membrane potential with potassium ions leaving the cell. Moreover, sodium channels are inactivated, further contributing to the repolarization of the membrane. The membrane potential then decreased below the resting potential, and slowly returns to the resting potential. The refractory period of neurons ensures the unidirectionality of propagating action potentials, and is a consequence of the inactivation of sodium channels.

2.3 Probing neuronal function

The latest advances in electrophysiology and optical imaging techniques are paving the way for increasingly advanced studies on the architecture and dynamics of biological neuronal networks. By combining single-cell and millisecond resolution, novel neurotechnologies allow to precisely monitor and manipulate neuronal activity, both *in vitro* and *in vivo* [38]. Electrophysiological techniques are the gold standard for the interrogation of neuronal circuits.

Patch-clamp directly measures intracellular signals at the subcellular level (**Figure II-3**). Although it exhibits exceptional signal-to-noise ratio, this method is highly invasive and its use is limited to a few neurons [39].

Microelectrode arrays (MEAs) can simultaneously record the activity of hundreds to thousands of neurons by embedding multiple closely spaced electrodes in a single device (**Figure II-3**) [38]. These platforms provide a minimally invasive extracellular recording method suitable for long-term experiments. The intracellular activity of neurons generates extracellular changes in the electrical charge distribution that are captured by nearby extracellular electrodes. Commercially available MEAs cover a broad range of applications, featuring different electrode layouts and spatial densities. Conventional passive MEAs are limited to 256 electrodes with an electrode pitch in the order of 100 µm (**Figure II-3** from [40]). Complementary metal-oxide semiconductor (CMOS) technologies now enable the integration of large arrays of recording electrodes along with integrated readout circuits on a single chip. Active CMOS-based MEAs can achieve high spatial resolution by reducing the number of required interconnections between electrodes and readout channels using multiplexing techniques [41], [42]. Neuropixels high-density probes based

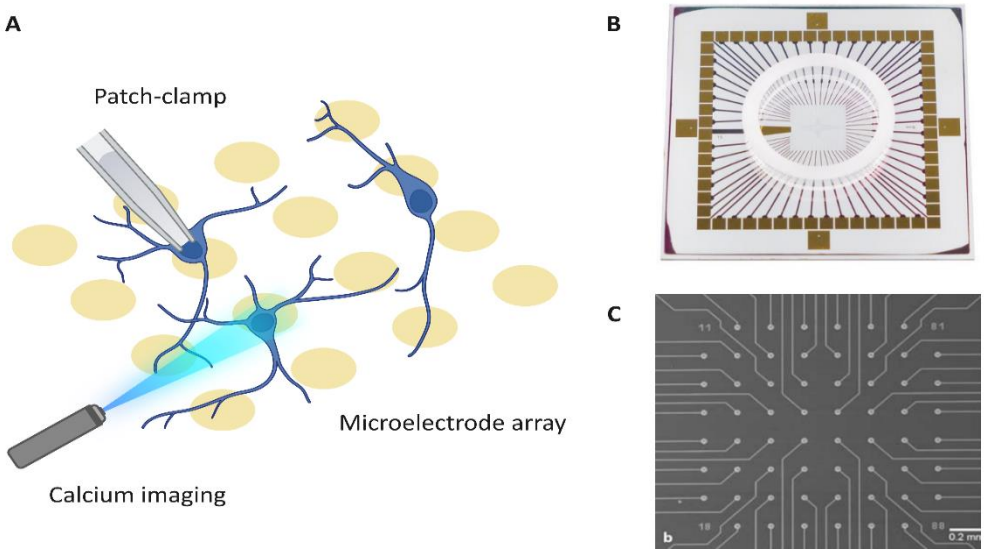

Figure II-3. Neuronal recording techniques. (A) Tools for probing neuronal circuits are depicted, including patch-clamp, microelectrode arrays and calcium imaging. (B) A planar 60-electrode microelectrode array (Multi Channel Systems MCS GmbH, Reutlingen, Germany) is shown; electrodes are located within the ring. (C) The electrode grid comprises 60 recording electrodes connected to the respective contact pads (not shown) through conducting wires [40].

on CMOS technology were designed for *in vivo* recordings across multiple brain regions, featuring 384 readout channels that can be configured to record from 960 selectable electrodes [43].

High-density microelectrode arrays (HD-MEAs) pose significant challenges for data analysis [44]. The high-dimensional datasets generated by modern recording techniques require outstanding computational processing capabilities to decode brain function from an increasingly larger number of simultaneously recorded neurons. Spike sorting extracts single-neuron spiking activity from extracellular recordings based on the characteristic spike waveforms produced by each neuron [45]. These algorithms are particularly relevant when dealing with high-density multi-unit recordings since each electrode can capture the activity of several neurons in its vicinity, and the activity of each neuron can be acquired by multiple nearby electrodes. Therefore, the growth in the number of recorded neurons calls for more robust and fully automated spike sorting techniques.

Calcium imaging offers a reliable alternative to the traditional electrophysiological methods (**Figure II-3**). In the nervous system, calcium signalling pathways regulate various neuronal processes, including synaptic integration and neuronal plasticity [46]. Fluorescent calcium indicators capture the intracellular calcium dynamics and provide an indirect measurement of neuronal activity. Wide-field calcium imaging enables large-scale simultaneous recordings of

thousands of neurons at the cellular level. However, fluorescence signals lack temporal resolution to resolve single spike events.

2.4 Summary

Neurons are the basic building blocks of the nervous system. However, the rich repertoire of neuronal dynamics emerging from neuronal populations is primarily determined by their ability to communicate with each other and form highly complex and dynamic networks.

Neuronal communication relies on the propagation of electrochemical signals within and between neurons. The active properties of the neuronal membrane support the initiation and propagation of action potentials and enables to effectively carry neuronal information over long distances.

In vitro cultured neurons coupled to high-resolution microelectrode arrays (MEAs) represent a relevant experimental model to study signal transmission in the nervous system and investigate the fundamental principles governing the organization of neuronal populations.

In the following chapter, computational methods to infer connectivity from neuronal activity recordings are discussed. These algorithms allow to characterize complex neuronal interactions and, ultimately, reveal key pathways involved in neuronal communication.

Chapter III

Connectivity inference

In this chapter, computational methods to infer connectivity in biological neuronal networks are reviewed, with a special focus on correlation-based metrics. The intuition behind each method is presented, along with the corresponding strengths and limitations. Moreover, the relevance of pre- and post-processing steps is briefly discussed.

In neuroscience, connectivity studies address multiple temporal and spatial scales [47], ranging from less than one millisecond and a few micrometres, at the synaptic level [48]–[50], to years and several centimetres, for circuit-level processes [51]–[53]. Depending on the research question, connectomes can be studied at the microscale between individual neurons, at the mesoscale within and between local neuronal populations, and at the macroscale across the whole brain [47]. The characterization of neuronal dynamics across multiple scales provides further insights into the complex associations between brain processes, occurring over months to years, and electrophysiological findings with subcellular resolution. Brain connectivity is evaluated at three distinct levels: structural, functional and effective connectivity [15], [24].

Structural connectivity, or anatomical connectivity, corresponds to the physical connections between neuronal elements (**Figure III-1**) [15]. Synapses are the anatomical structures that mediate the interactions between neurons. Although these connections are relatively static over short time scales, structural plasticity is particularly relevant during development and learning processes [32], [54], through the physical deletion and creation of synapses. Structural maps obtained with electron microscopy are able to capture connections at the subcellular scale; in [55], the complete nervous system of the nematode *Caenorhabditis elegans*, composed of 302 neurons, was described for the first time. However, this task becomes impracticable for large-scale neuronal networks featuring thousands of neurons [56].

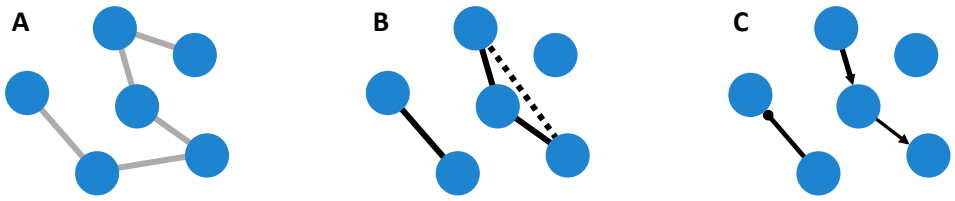

Figure III-1. Types of connectivity. (A) Structural connectivity. (B) Functional connectivity. (C) Effective connectivity.

Functional connectivity refers to the statistical dependence between the activity of two neuronal elements [15]. Two units are functionally linked if the activity in one of them influences the probability of firing of the other, without considering any causal effects. Functional connectivity maps are derived from neuronal activity recorded using electrophysiology techniques [57] and neuroimaging methods, such as calcium imaging [57], [58] and fMRI [52]. Synaptic plasticity refers to the adaptation of synaptic efficacy between neurons depending on the neuronal activity level [54]. By encoding the extent of interaction between pairs of neurons, functional connectomes are able to capture these changes in synaptic strength.

Despite the points of communication provided by synapses, a physical connection does not always translate into a functional interaction, and vice-versa (**Figure III-1**). A physical connection may not be detected when the source neuron exhibits reduced activity, or the target neuron is strongly inhibited by other neurons [24]. On the other hand, a functional connection between two neurons that are not directly connected can be inferred if they share a common input or interact through a third unit [24]. Although there is not a perfect match between structural and functional connectivity maps, functional connectomes are largely constrained by the anatomical structure, retaining key features of the architecture of neuronal networks [59], [60].

Finally, **effective connectivity** describes the interactions between neuronal units as causal events, where the activity of a given unit directly affects the activity of another unit [15], [61], under a causal model. Besides the strength, effective connections are characterized by their directionality and latency: the source and the target units are identified along with the delay associated with their interaction. In addition, excitatory and inhibitory effects can be distinguished depending on whether the target unit is triggered or silenced by the source unit, respectively (**Figure III-1**).

3.1 Data processing pipeline

Electrophysiological techniques and neuroimaging methods are the standard approaches to record neuronal activity [62]. The need for a pre-processing stage prior to connectivity inference depends on the recording method and the input requirements of the connectivity inference algorithm. Although voltage time series allow to directly infer networks [63], spike trains are usually derived

using spike detection algorithms. Spike trains encode neuronal data by preserving the most relevant information: the neuronal firing timings.

Regarding electrophysiological data, current technologies allow to record neuronal activity with subcellular resolution. In multi-electrode recordings, a single electrode can capture the activity of multiple neurons, and the same neuron can be detected by different electrodes. Spike sorting algorithms are able to separate spikes from different sources [45], and hence connectivity can be assessed between individual neurons. On the other hand, neuronal activity acquired with neuroimaging techniques requires the transformation of a temporal sequence of images into a time series of neuronal activity for each identified neuron. This procedure involves an image segmentation to identify the regions of interest, followed by the extraction of the fluorescence time series for each neuron [24].

Generally, the neuronal activity data can be expressed as,

$$D = \{x_i(t) | i = 1, \dots, N; t = 1, \dots, T\} \quad [10]$$

where $x_i(t)$ refers to the neuronal activity of unit i at time t [24]. The variable $x_i(t)$ is continuous for raw data, whereas it is binary when spike trains are extracted from the data.

After pre-processing, the choice of the algorithm to infer connectivity should consider the level of detail required for the specific application and the computational resources available. Connectivity inference methods are broadly classified into model-free and model-based algorithms based on their mathematical foundations [24]. Model-free methods rely on descriptive metrics and do not require any assumption on the process generating the data – non-parametric methods. On the other hand, model-based approaches adopt generative models to reproduce the dynamics of neuronal networks by fitting the model parameters to the data – parametric methods. These algorithms provide a mechanistic view of the neuronal dynamics. Moreover, generative models can be used to simulate neuronal data for model validation [64]. Although model-based methods allow to model more complex aspects of the neuronal dynamics, the increasing number of parameters may limit the applicability of these models [24].

The connectivity inference problem can be addressed using different approaches but, ultimately, each one of these methods yields a $N \times N$ connectivity matrix, $CM = [\, c_{ij} \,]$, where N is the number of neurons, neuronal assemblies or brain regions, depending on the spatial scale, and c_{ij} represents the strength of the connection between any two units i and j. When interactions are evaluated at the synaptic level, c_{ij} corresponds to the synaptic weight between two neurons i and j, and the synaptic weight matrix is derived.

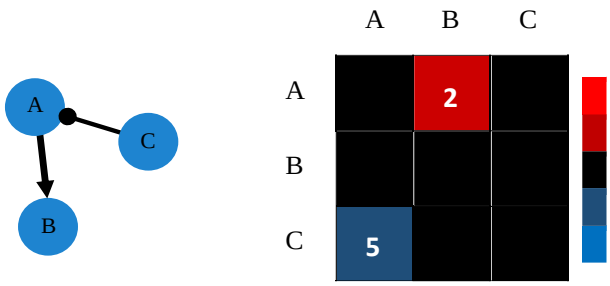

Figure III-2. Connectivity matrix. The corresponding connectivity matrix is obtained for a set of units (A, B and C). The strength of each connection is color-coded (red for excitatory connections and blue for inhibitory connections), and their latency is also represented.

Depending on the network inference algorithm, connectivity matrices are able to capture different levels of detail of the neuronal networks. The value assigned to the strength of the connection, c_{ij}, can either be binary, only providing information on the presence or absence of interaction between the units, or continuous, containing information on the strength of the connection. The diagonal elements of the matrix are zero, since autapses (self-synapses) are usually not considered. Acausal indicators provide symmetric matrices since the directionality cannot be derived. On the other hand, directed connectivity methods allow to assess the directionality of connections and identify the reference and target units involved in the connection, and a delay matrix can be obtained as $DM = [\,\tau_{ij}\,]$, where τ_{ij} represented the delay between units i and j.

These methods result in a square connectivity matrix. Each entry represents the strength between units. Even when no significant interaction exists, a value is obtained. The question is how significant connections can be distinguished from non-significant one. Neuronal networks are known to be sparse connected, featuring more non-significant links. This distribution of weights can then be obtained, and a thresholding method can be used to differentiate the connections [65].

Different thresholding methods have been described. Hard thresholding is based on the mean and standard deviation of the distribution of weights, assuming that stronger connections are present in lower quantity and present significant higher values. Considering all connections is usually not appropriate since excitatory and inhibitory interactions are assigned different ranges of values. Therefore, different thresholds are calculated for each type [66].

Density-based thresholding assumes a fixed density of connections, that is, after sorting the obtained links, only the M strongest connections are kept. This can be misleading since biological networks are highly variable depending on the level of development and the location [65].

Double thresholding was introduced because some connections may not present high values, but they are still significant given its neighbourhood. After a first threshold, similar to the one used in hard thresholding, the rejected connections are further assessed, and a new threshold is obtained

for each row. If a weight exceeds this threshold, the corresponding connection is considered significant [65].

More complex approaches to assess the significance of connections can be used, such as shuffling methods. From the original data, a surrogate dataset is obtained by destroying all correlation between spike trains when events are randomly relocated. These second matrix can then be used to compare with the original one, and check if they largely differ. However, this method is computationally expensive, and the results are not so different from what is obtained with thresholding methods [65].

3.2 Model-free methods

Correlation and information theory concepts are widely applied in connectivity inference problems [67]. These metrics provide an estimate of the connection strength based on general mathematical concepts, without imposing any particular distribution for the data.

Erro! A origem da referência não foi encontrada. and *Table III-2* summarize the main model-free methods, highlighting their strengths and limitations. Representative studies are listed for each method.

3.2.1. Correlation-based methods

Statistical correlation measures the strength of the linear relationship between two random variables. In the context of network inference, these variables represent neuronal elements such as neurons, neuronal assemblies or brain regions [68]. A simple correlation between the spiking activities x_i and x_j of two units i and j conveys information about the rate of co-occurrence of spikes. The Pearson correlation coefficient is a commonly used metric to assess functional connectivity from neuronal data [69], and is defined as,

$$\rho_{ij} = \frac{\Sigma_{ij}}{\sqrt{\Sigma_{ii}\Sigma_{jj}}} \quad [11]$$

where Σ_{ij} is the covariance between units i and j. The coefficient values range from -1 to +1, where -1 indicates a strong negative linear relationship, which may reveal inhibitory interactions, +1 denotes a strong positive linear correlation, possibly associated with excitatory interactions, and 0 implies no linear dependency between units. However, details on the directionality of the connections are not captured.

Cross-correlation (CC) estimates the strength of the delayed linear relationship between two units i and j. The probability of observing a spike event in a target unit, j, at time $t + \tau$, given that a spike event in a reference unit, i, was detected at time t, is assessed by time-shifting x_j with respect to x_i by a fixed time delay, τ [66]. Mathematically, this is equivalent to the sum of the product between x_i and a delayed version of x_j, followed by normalization, as expressed below,

$$C_{ij}(\tau) = \frac{1}{\sqrt{N_i N_j}} \sum_{s=1}^{N_i} x_i(t_s) x_j(t_s - \tau) \quad [12]$$

where t_s corresponds to the timing of a spike event in x_i, and N_i and N_j represent the total number of spike events in x_i and x_j, respectively. The normalization approach presented here considers the total number of events for each unit to obtain an estimate between 0 and 1 [24], [66]. A normalized cross-correlation of 1 indicates that the firing of an event in i reliably triggers an event in j, with all the events detected in j being evoked by events in i. Although cross-correlation considers the spike train history to detect causal events, the time delay, τ, should be carefully selected to ensure that all the relevant connections are identified. Moreover, excitatory and inhibitory interactions cannot be distinguished since the output value is always a positive number.

A cross-correlogram allows to evaluate the cross-correlation between two random variables over a range of time delays, τ. Considering that an event in a given unit j is triggered by an event in another unit i if the maximum time delay between events is τ_c, a causality window can be defined as $\tau = [-\tau_c, \tau_c]$. The cross-correlation is computed between a defined reference unit, i, and a target unit, j, by sliding the activity of the target, x_j, relative to the activity of the reference, x_i, across the causality window. The cross-correlogram provides information about the interactions between i and j in both directions, with positive time delays referring to connections from i to j, and negative delays corresponding to connections from j to i.

The shape of the cross-correlogram reflects the relationship between the analysed spike trains. When two units are independent, the cross-correlogram is approximately flat within the causality window. On the other hand, if an excitatory interaction is present, the cross-correlation is able to detect an increase in synchrony between spike trains. Therefore, a peak appears at the corresponding time delay with an amplitude related to the degree of synchronization between the units. A functional connection is then identified based on the peak value of the cross-correlogram. A positive delay is obtained when the reference unit triggers the target unit, while a negative delay is observed otherwise [66].

Inhibitory interactions arise when the activity of a given unit i decreased the probability of firing of another unit j. These interactions are characterized by a trough in the cross-correlogram across a range of time delays where no activity in unit j is expected. Network inference algorithms report

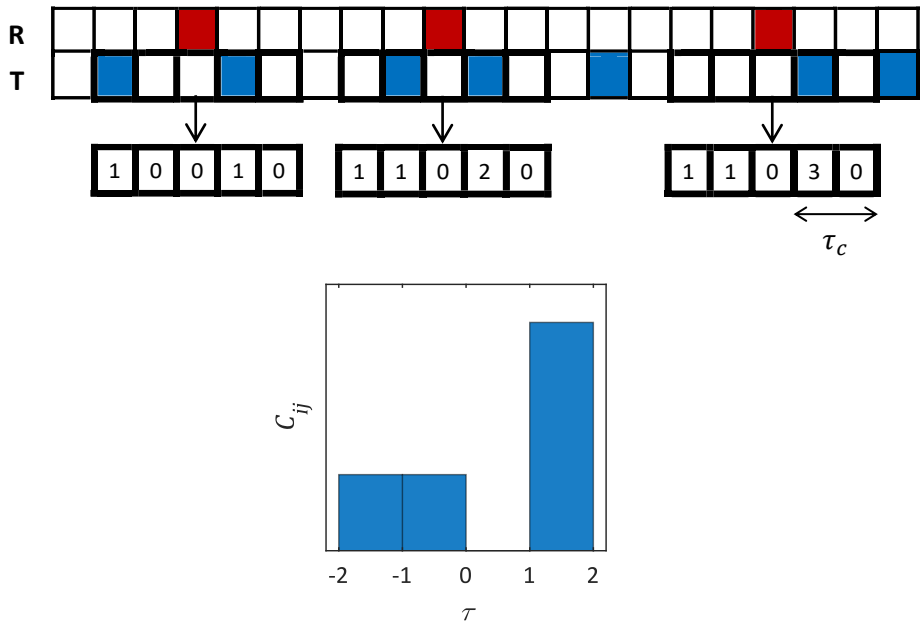

Figure III-3. Cross-correlation histogram. The connection between two spike trains R and T is evaluated, taking R as the reference train. A causality window is defined around each reference spike, and target spikes are identified. The corresponding time delays are represented in a histogram.

a lower sensitivity to inhibition relatively to excitation, mainly due to the low firing rates exhibited by *in vitro* neuronal cultures [66], [70]. The inhibitory effect is more readily observed when the target unit exhibits high baseline activity.

The cross-correlation histogram (CCH) allows to efficiently evaluate the dependence between two binarized spike trains by directly inspecting the spike timestamps [66]. The time delays between spikes are obtained and represented in the histogram (F). Besides the causality window, the bin width of the histogram is defined. Larger bin widths may filter out irrelevant noise in the distribution, whereas shorter bin widths may reveal more details and estimate the latency of interactions with more precision. Similar to the previous approach, functional connections are detected based on the peak value of the histogram. This procedure works well if the considered units share an excitatory link; however, inhibitory links, represented by throughs in the histogram, are not detected. A filtered version of the normalized cross-correlation histogram (FNCCH) was introduced to address this problem,

$$FNCCH_{ij} = argmax_{\tau}\left\{\left|C_{ij}(\tau) - \frac{1}{2\tau_c}\sum_{v=-\tau_c}^{v=\tau_c} C_{ij}(v)\right|\right\}. \quad [13]$$

The mean value of the cross-correlation between units i and j is calculated and subtracted from the normalized cross-correlation histogram, and the absolute value is obtained. The mean value represents the relative frequency of random interactions between the units. By subtracting this value, positive peaks appear when significant positive correlations are found above the baseline

level, and decreases in synchrony will be represented by negative values. By taking the absolute value of the filtered distribution, the largest peak or trough is identified, and the type of connection (excitatory or inhibitory) is assigned according to the original sign.

Partial correlation was introduced to deal with indirect effects by excluding the influence of all other units when assessing the strength of the connection between a pair of units [71]. Indirect effects correspond mainly to polysynaptic connections, where the apparent interaction between two units is accomplished through a third unit. Another common example of apparent connections is the existence of a common input, which can be either another unit or an external variable (*i.e.*, an external stimulus). However, this method is computationally expensive, and it requires additional steps to extract more information about the identified connections, such as the latency and directionality.

The intuitiveness and low computational costs involved in the computation of these correlation-based metrics are an advantage and that is why they are widely used to tackle the connectivity inference problem. However, correlation is an intrinsic linear operation and, thus, only linear relationships between units can be detected. One can question if this is enough to describe such complex systems as neuronal networks. Although it is certainly not enough, it proves that relevant information can be extracted using simple tools. In the following sections, methods capable of capturing non-linear relationships between spike trains are described.

Finally, the values that are attributed to each connection in the connectivity matrix should provide a clear estimate of the strength of the connection. Establishing a meaningful and widely applicable range for the computed weights, with improved robustness to background noise and variances in firing rates, is a key step towards a more generic framework for connectivity inference analysis. Normalization constants are usually adopted, but they still lack the ability to assign the same weight to connections where differences rely on factors external to their interaction.

3.2.2. Information theoretic methods

Interactions between neuronal elements can be interpreted as dynamic channels, allowing information to flow across units. In the information theory field, several metrics were introduced to quantify the transmission of information in communication systems, which can also be applied to infer connectivity in neuronal circuits. Information entropy is a core concept in information theory, providing a mathematical definition to measure the information content of a random variable. Non-linearities between spike trains can be captured.

Mutual information (MI) measures the mutual dependence between variables, such as spike trains. In other words, it can be interpreted as the amount of information that can be extracted from a

random variable by observing another random variable. In the context of connectivity inference, this means that we can predict the activity of a given unit by observing other units within the network. However, this is a symmetric metric, thus, unable to identify the directionality and latency of interactions [24].

The joint entropy (JE) of two random variables can be used to infer connectivity between two units by testing whether a reference unit is a cause of activity in a target unit. The cross-inter-spike-intervals (cISI) distribution is obtained, and the joint entropy is computed as the entropy of the histogram. The lower the JE value, the stronger the connection between the considered units since the distribution presents a sharper peak, possibly related with a functional connection. Although it provides a different approach to solve the connectivity inference problem, JE presents the same issues as MI [24].

All the approaches above are only able to estimate the strength of the dependence between two units. In order to extract more information about these interactions, transfer entropy has been recently adopted since it allows to detect causal relationships by considering the spike train history. Transfer entropy (TE) is defined as a measure of flow of information between two random processes. However, this metric only considers as past history the immediately preceding time bin. Some variations of TE have been implemented in an attempt to include more information about the past activity. Delayed transfer entropy (DTE) considers a delayed version of the source signal for the computation. Still, only a past time bin is considered. High order transfer entropy tries to include more information at a higher cost by taking into account multiple time bins in the past. Although more information can be extracted using transfer entropy concepts, this metric is still not able to distinguish excitatory and inhibitory connections or identify indirect effects [72], [73].

Similar to correlation-based approaches, information theoretic concepts rely on the individual assessment of each possible combination of units. As the number of electrodes increase, these analyses can rapidly become impractical. Also, the range of values is not fixed.

3.2.3. Supervised learning

A new interest in supervised learning approaches to tackle the connectivity inference problem has arisen with the emergence of deep learning networks capable of dealing with the increasing number of electrodes available for recording. However, the requirement for a ground truth to train these models hamper the application of these strategies since the processes to generate labelled data is tedious and almost impractical for large-scale neuronal networks. The potential of these approaches can be explored by taking advantage of simulated *in silico* networks, for which the structural connectivity matrix is known a priori [24].

3.3 Model-based methods

Generative models are obtained from raw data to reproduce the dynamics of neuronal circuits. A more or less realistic model of the network is obtained and information such as connectivity inference can be extracted by observing its behaviour [24]. However, such model-based approaches require to impose a model for the generation of data, which is usually not known.

3.4 Graph theory

Neuronal networks can be described by weighted directed graphs G = (V,E), where V corresponds to the set of nodes (neuronal units, in this case) in the network and E is the set of directed connections between the units. Each connection is assigned a weight based on the strength of interaction between nodes. These values can also be represented in an adjacency matrix, which corresponds to the connectivity matrix [74].

Assuming a graph representation, a number of metrics can be extracted to characterize the architecture of networks.

The cluster coefficient is one of the most commonly used metrics and, for each node, is obtained by computing the ratio between the number of actual connections between the neighbours of the node and the number of all possible connections between them. This allows to quantify the level of segregation of the network and investigate possible clusters with higher levels of activity [75].

The degree of each node is given by the number of connections where the node is either a source or a target. If we consider only the incoming or outcoming connection, the in-degree and out-degree can be computed, respectively. The degree of a node gives information about the extent to which this node affects the network. When a node presents a degree that is, at least, one standard deviation above the average degree, it corresponds to a hub node. Hub nodes are important since they extensively affect the dynamics of the networks [75].

3.5 Summary

Understanding the architecture of neuronal circuits is a crucial step towards elucidating the neuronal mechanisms underlying brain function. By exploiting the potential of high-resolution neuronal data, connectivity studies are opening up new opportunities for characterizing neuronal connections at multiple temporal and spatial scales – functional connectivity –, and unravelling the complex dynamics of neuronal communication pathways – effective connectivity.

Several algorithms have been described to address the connectivity inference problem. Selecting the most appropriate method relies on the level of detail required for each specific application and the availability of computational resources. Correlation-based algorithms provide a simple yet effective tool to reconstruct neuronal circuits by capturing the magnitude and causality of neuronal interactions.

Overall, the connectivity inference methods reviewed here are implemented in batch mode. However, an online approach may prove valuable in studying how neuronal dynamics affect network inference with single-event resolution, and deriving connectomes from real-time neuronal data.

In the following chapters, a novel methodology to estimate directed connectivity in biological neuronal networks is presented. Besides identifying excitatory and inhibitory links based on cross-correlation metrics, an online implementation is proposed to infer the corresponding connectivity matrix as new events are detected.

Table III-1. Correlation-based methods for connectivity inference.

Method	Principle	Features	Limitations
Correlation	Strength of the linear relationship between two random variables [15].	Linear relationship between spike trains.	No standard definition. Limited to linear relationships. Acausal indicator. Does not distinguish excitatory and inhibitory connections. Does not discriminate between direct and indirect effects.
Cross-Correlation (CC)	Strength of the delayed linear relationship between two random variables.	Linear relationship between spike trains. Causal indicator.	Limited to linear relationships. Does not distinguish excitatory and inhibitory connections. Does not discriminate between direct and indirect effects.
Cross-Correlation Histogram (CCH)	Evaluates the cross-correlation between two random variables over a correlation window [76], [66].	Linear relationship between spike trains. Causal indicator.	Limited to linear relationships. Does not discriminate between direct and indirect effects. Lower sensitivity to inhibitory connections.

		Some variations allow to detect excitatory and inhibitory effects.	
Partial Correlation (PC)	Strength of the linear relationship between two random variables, excluding the effects of all other variables [71].	Linear relationship between spike trains. Discriminates direct and indirect effects.	Limited to linear relationships. Acausal indicator. Does not distinguish excitatory and inhibitory connections. Computationally expensive.

Table III-2. Information theory methods for connectivity inference [24].

Method	**Principle**	**Features**	**Limitations**
Mutual Information (MI)	Amount of information that can be obtained from a random variable by observing another random variable.	Non-linear relationship between spike trains.	Acausal indicator. Does not distinguish excitatory and inhibitory connections. Does not discriminate between direct and indirect effects.
Joint Entropy (JE)	Tests whether a reference neuron is a cause of activity in a target neuron by	Non-linear relationship between spike trains.	Acausal indicator.

	computing the cross-inter-spike-intervals (cISI).		Does not distinguish excitatory and inhibitory connections. Does not discriminate between direct and indirect effects.
Transfer Entropy (TE)	Measure of flow of information between two random processes.	Causal indicator. Non-linear relationship between spike trains.	Does not distinguish excitatory and inhibitory connections. Does not discriminate between direct and indirect effects.
Delayed Transfer Entropy (DTE)	Same as TE but considering a delayed version of the source signal.	Causal indicator. Non-linear relationship between spike trains.	Does not distinguish excitatory and inhibitory connections. Does not discriminate between direct and indirect effects.
High Order Transfer Entropy (HOTE)	Same as TE but considering multiple time steps of activity.	Causal indicator. Non-linear relationship between spike trains.	Does not distinguish excitatory and inhibitory connections. Does not discriminate between direct and indirect effects.

Chapter IV

Materials and methods

In this chapter, computational and experimental strategies to investigate network connectivity in neuronal assemblies are detailed. Synthetic data was generated using simple computational neuronal models for subsequent algorithm validation. Compartmentalized microfluidic devices were also explored to engineer neuronal circuits *in vitro* with defined architectures. Finally, an experimental protocol was designed to provide "real-time" information on network connectivity from neuronal cultures coupled to microelectrode arrays.

4.1 Synthetic spike train data

Synthetic data is a valuable tool to formulate and validate research hypotheses before acquiring and analysing real data. The stochastic nature of neuronal firing can be described by a Poisson point process. A Poisson point process is a type of stochastic process that is widely used for modelling discrete events occurring independently at a certain rate λ. The time differences between the events are known as interarrival times τ and follow an exponential distribution with mean $\bar{\tau} = 1/\lambda$ [77].

Each spike train was generated in MATLAB (R2022b, The MathWorks, Inc., Natick, MA, USA) by creating an array of N random numbers drawn from an exponential distribution with mean $\bar{\tau}$, which correspond to the interarrival times between events. The mean interarrival time $\bar{\tau}$ and the total number of events N were varied to simulate neurons with different activity levels.

4.2 NEURON simulations

From basic cellular mechanisms supporting neuronal function to information encoding at network level, computational neuroscience provides a theoretical and mathematical framework to address the most compelling research questions in the field of neuroscience. The NEURON simulation environment is a widely used open-source tool for modelling and simulating neuronal dynamics from single neurons to complex neuronal networks [78]. Over the years, neuronal recording data has driven the implementation of empirically-based models to bridge the gap between theory and experimental findings. NEURON offers a powerful platform to build biologically realistic quantitative models with great control over the morphology and biophysical properties of neuronal populations.

NEURON supports programming in HOC, an object-oriented programming language with a C-like syntax, and, more recently, in Python. Moreover, a graphical user interface (GUI) enables to conveniently build and manage neuronal models, control simulation parameters and plot variables as a function of time and space, without having to write any code (**Figure IV-1**) [79].

Sections are the basic structural units in NEURON. Biophysical ("realistic") cell models combine multiple cylindrical sections to form any tree-like topological structure. Each section is assigned morphological and biophysical properties using the CellBuilder graphical tool. Morphological properties include the length, L, and the diameter, d, of the section. Biophysical properties comprise the axial membrane resistivity, Ra, the specific membrane capacitance, cm, and other biophysical mechanisms, such as ion channels. NEURON provides a few built-in biophysical mechanisms, but additional mechanisms written in NMODL language can be specified by the users. Published model descriptions are publicly available from online databases, namely ModelDB [80].

Biophysical mechanisms are governed by sets of algebraic and/or differential equations and kinetic schemes [81]. The membrane potential and gating states of biophysical model neurons are derived using numerical integration methods. On the other hand, artificial cell types provide simple and computationally efficient models based on Poisson processes (NetStim objects) and integrate-and-fire neurons (IntFire objects) with analytical solutions [82].

Synapse objects (*i.e.*, ExpSyn) are attached to pre-existing cell models at a chosen section. Each synapse is characterized by its reversal potential, e, and its decay time constant, τ_{syn}. The synaptic reversal potential, e, is defined by the type of neurotransmitters released from the presynaptic neuron, and determines the evoked postsynaptic potential: a reversal potential above the membrane resting potential depolarizes the postsynaptic membrane, thereby increasing the probability of a postsynaptic action potential firing – excitatory synapse –, whereas a reversal

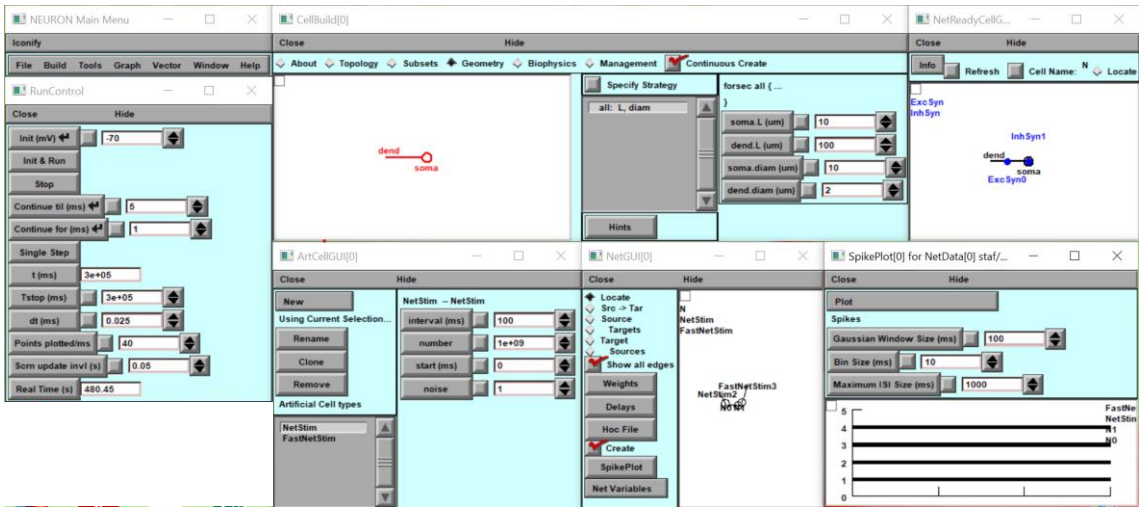

Figure IV-1. NEURON's graphical user interface. NEURON provides a set of interactive graphical tools (panels) to build and simulate single neurons and networks of neurons with minimal programming experience.)

potential below the membrane resting potential hyperpolarizes the postsynaptic membrane and reduces the likelihood of a postsynaptic action potential occurring – inhibitory synapse [83]. Exponential synapses (ExpSyn) are event-driven synapses with a discontinuous change in conductance, G, followed by an exponential decay with time constant tau,

$$i = G \cdot (v - e) \qquad [14]$$

$$G = w \cdot e^{-\frac{t}{\tau_{syn}}} \qquad [15]$$

where i is the synaptic current and v refers to the membrane potential. The weight, w, is the peak amplitude of the synaptic conductance, and is defined by a Network Connection (NetCon) object. NetCon objects establish synaptic connections between a spike source, including both biophysical and artificial cell types, and a synaptic target (*i.e.*, ExpSyn). Besides the source and the target, the synaptic weight, w, the synaptic delay, τ, and the threshold for spike detection are specified for each connection. When the source potential exceeds the threshold at a given time t, an event is triggered in the target at time $t + \tau$.

In silico modelling of biological neuronal networks using neuroscience simulators such as NEURON is particularly relevant in the context of network inference. Simulated neuronal networks with known connectivity given by the synaptic weight matrix (SWM) provide ground truth data for algorithm validation.

Simple network models composed of two biophysical cells were created. More complex networks were not required since the final goal relies on the paired interaction between pairs of neurons. Each neuron was represented by a two-compartment cell consisting of a soma (ball) and a dendrite

Table IV-1. Morphological properties of biophysical model neurons presented by neuronal compartment.

Soma		**Dendrite**	
length, L (µm)	**diameter, d (µm)**	**length, L (µm)**	**diameter, d (µm)**
10	10	100	2

Table IV-2. Biophysical properties of biophysical model neurons presented by neuronal compartment.

		Soma	**Dendrite**
Axial resistivity, Ra (Ω·cm)		150	150
Specific membrane capacitance, cm (µF/cm^2)		1	1
Passive channels	g_pas (S/cm^2)	0.001	0.001
	e_pas (mV)	-70	-70
Hodgkin-Huxley sodium, potassium and leak channels	$gnabar\_HH2$ (S/cm^2)	0.1	-
	$gkbar\_HH2$ (S/cm^2)	0.06	-
	$vtraub\_HH2$ (mV)	-55	-

(stick) – ball-and-stick model. For this model, the axonal compartment is not explicitly modelled. Signal propagation along the axon is considered by introducing a delay between spikes detected in the soma of the presynaptic neuron and synaptic events triggered in the postsynaptic neuron.

Table IV-1 and **Table IV-2** present the morphological and biophysical parameters describing the biophysical neurons. Each cell compartment was modelled as a cylindrical structure. A single apical dendrite of 100 µm in length and 2 µm in diameter emerges from the soma with a length and diameter of 10 µm, which is consistent with typical measurements in the nervous system [84]. The number of segments was set to 1 for both structures. Passive properties were inserted in the somatic and dendritic membranes, including axial resistivity (R_a = 150 Ωm, from [85]), specific membrane capacitance (c_m = 1 µF/cm^2, from [85]), and leakage channels ("pas" mechanism) with a reversal potential of -70 mV and a maximum conductance equal to 0.001 S/cm^2 (default parameters), contributing to the resting membrane potential. Fast Na^+ and K^+ currents for action potential generation based on the Hodgkin-Huxley model were added to the soma ("HH2" mechanism for hippocampal neurons, from [86] and adapted from [87]). Although dendrites also express voltage-gated ion channels, several studies suggested that passive properties are sufficient to support synaptic integration and signal propagation in dendrites [88], [89]. Here, dendrites were modelled as purely passive compartments since our focus relies on the output-output interaction between pre- and post-synaptic units, rather than synaptic-level computations.

Table IV-3. Parameters for each simulated networks in NEURON.

Network	Type of connection	Mean interarrival time – source (ms)	Mean interarrival time – target (ms)
1	excitatory	100	100
2	excitatory	100	1
3	excitatory	1	100
4	inhibitory	100	100

Excitatory (e = 0 mV and tau = 5 ms, for AMPA-like receptors) and inhibitory (e = -80 mV and tau = 10 ms, for $GABA_A$-like receptors) synapse objects were attached to the dendrite and soma of each neuron, respectively. The slower kinetics of inhibitory synapses is reflected on a larger decay time constant [90], [91].

Each biophysical model neuron was triggered by an artificial cell (NetStim) with a defined mean interarrival time, $\bar{\tau}$. These connections were established via a NetCon object, where the source was an artificial cell, and the target corresponded to an excitatory synapse in each biophysical cell. The synaptic weight was selected as the minimum value to consistently trigger an event in the target upon an event in the source (w = 0.008 and τ = 0 ms). Excitatory and inhibitory links between biophysical model neurons were established considering different synaptic weights and a synaptic delay, τ, equal to 2 ms. Different firing rates for each cell were simulated by changing the mean interarrival time, $\bar{\tau}$, of the corresponding artificial cell. Each network (*Table IV-3*) was simulated for a range of different weights (0.001, 0.002, 0.005, 0.0055, 0.006, 0.0065, 0.007, 0.0075, 0.0078, 0.008, for excitatory and 0.00001, 0.00002, 0.00005, 0.0001, 0.0005, 0.001, for inhibitory), and repeated 5 times. Each run simulated 5 min and 10 min of spontaneous activity for excitatory and inhibitory links, respectively. All simulations were carried out at 37ºC.

For each trial, the voltage traces and spike trains regarding each simulated biophysical cell were exported and stored for offline analysis in MATLAB.

4.3 Real electrophysiology recordings

4.3.1. Engineering controlled neuronal circuits

In vitro patterned neuronal circuits based on 3D structural confinement provide a versatile tool to study how network architecture affects the spatiotemporal activity patterns expressed by neuronal cultures. These microstructures allow to selectively isolate different cell types and neuronal compartments based on geometric features. Unidirectional neurite growth can be achieved with

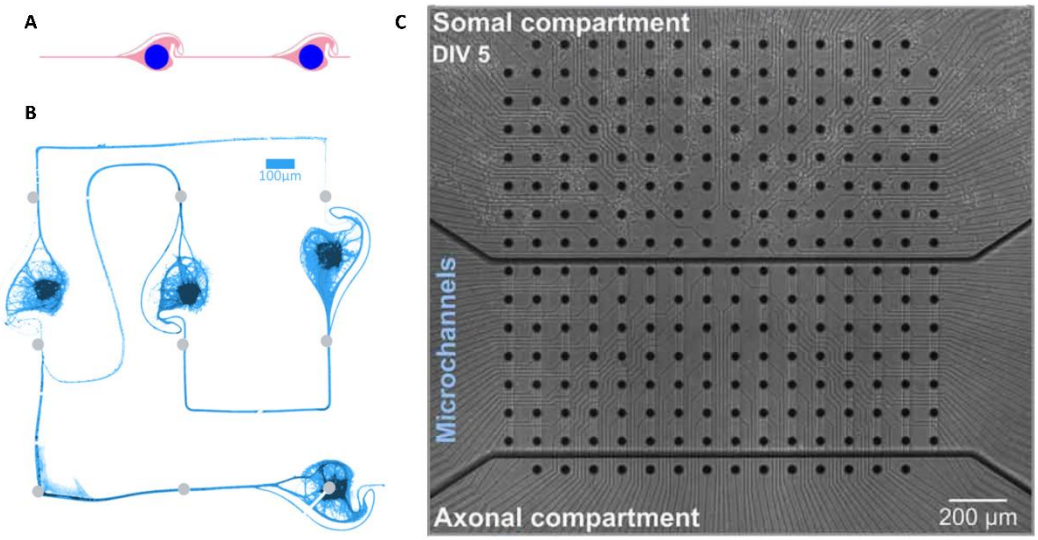

Figure IV-2. *In vitro* patterned neural circuits. (A) 'Stomach' motif used for the assembly of the microcircuit in (B). (B) Unidirectional circuits composed of several 'stomach' motifs [92]. (C) Phase-contrast microscopy image of a primary hippocampal neuronal mono-culture at 5 DIV. The microelectrode array active area is shown (10× objective, mosaic). A microfluidic device composed of 16 microchannels (10 µm width; 700 µm minimum length) is aligned to include seven microelectrodes each [93].

asymmetrical designed channels featuring a preferred growth direction [92]. Therefore, engineered networks offer a great control over the topological motifs exhibited by neuronal cultures, as opposed to randomly connected homogeneous networks, and thus constrain functional information flow through networks with high reproducibility. Functional connectivity analysis based on neuronal activity recordings enable to assess signal transmission efficiency between compartmentalized (sub-)cellular structures. Here, two distinct designs were tested: a modular microstructure based on stomach-like structures and a two-compartment system with connecting microchannels.

A modular microstructure composed of four directional circuits with 4 nodes each was designed to build small-scale, multi-node networks with unidirectional connections. Neuronal cells are seeded into the nodes (**Figure IV-2**). The nodes feature an asymmetrical stomach-like structure that guides neurite growth (from right to left) relying on the tendency of neurons to avoid sharp turning angles. Two additional bidirectional circuits of straight channels were used as reference [93].

A two-compartment microfluidic system composed of two chambers (somal and axonal) interconnected by 16 microchannels with 700 µm in length, 10 µm in height, and 10 µm in width was designed to investigate signal propagation characteristics of axons (**Figure IV-2**). The initial

cell plating is performed onto the somal compartment, and axons are allowed to growth along the microchannels and reach the axonal compartment. The length of the microchannels was selected so that axons were the only structures capable of reaching the axonal compartment, as a length of 450 μm is enough to restrict the access to axons only. The width of the microchannels allowed to maintain soma-exclusion properties and restrict the number of axons accommodated per microchannels, achieving a lower complexity of the signal recorded from electrodes placed under these structures [94].

Compartmentalized microfluidic devices (CMDs) enable to access (sub-)cellular structures. By combining microElectrode arrays and microFluidics (μEFs), neuronal cultures with well-defined functional connectivity can be probed with high spatiotemporal resolutions.

4.3.2. Substrate preparation

Polydimethylsiloxane (PDMS) was used in the fabrication of the compartmentalized microfluidic devices described in the previous sub-section. Due to its high versatility in the design of 3D microstructures with nanoscale resolution, and excellent biocompatibility, optical transparency and gas permeability properties, PDMS has been extensively exploited to engineer biologically relevant neuronal networks *in vitro*. Soft lithography is a standard microfabrication technique for polymer-based microfluidic systems, such as PDMS microfluidic devices. Briefly, topographically patterned surfaces are produced by replica molding from a photoresist-based master mold [95].

For the multi-node networks, planar MEAs (60MEA500/30iR-Ti-gr, Multi Channel Systems MCS GmbH, Reutlingen, Germany) of 60 titanium nitride (TiN) electrodes (59 recording electrodes and one internal reference electrode) 500 μm spaced with a diameter of 30 μm and arranged in a 6 by 10 rectangular grid were used. The circuit structures were aligned with the microelectrode grid, and each circuit encompassed 9 electrodes in a 3 by 3 square grid (). The μEFs were air plasma-cleaned for surface hydrophilization, and then coated with poly-D-lysine, thereby providing a culture substrate with enhanced cell-adhesive properties [93].

For the two-compartment microfluidic system, planar MEAs (256MEA100/30iR-ITO-gr, Multi Channel Systems MCS GmbH, Reutlingen, Germany) constituted by 256 TiN electrodes (252 recording electrodes and four internal reference electrodes) 100 μm spaced with a diameter of 30 μm and organized in a 16 by 16 square grid (electrodes in the four corners were not present) were used. The number of microchannels (16 microchannels in total) matched exactly the number of microelectrode columns. Thus, precise alignment between the microfluidic system and the microelectrode grid enabled to probe each microchannel with seven vertically aligned, equally

spaced electrodes (**Figure IV-2**). Similarly, the assembled μEFs were air plasma-cleaned, and subsequently coated with the adhesion proteins poly-D-lysine and laminin [94].

Additional experiments without topological constraints were carried out on planar MEAs (60MEA200/30iR-Ti-gr, Multi Channel Systems MCS GmbH, Reutlingen, Germany) of 60 TiN electrodes (59 recording electrodes and one internal reference electrode) 200 μm spaced with a diameter of 30 μm and arranged in an 8 by 8 square grid (electrodes in the four corners were not present). Substrate preparation followed the procedure presented above.

4.3.3. Cell culture

Dissociated primary hippocampal neurons (PHN) from Wistar rat embryos at embryonic day 18 (E18) were cultured in Neurobasal (Plus) medium supplemented with penicillin-streptomycin.

For the multi-node networks, cells were seeded onto the microstructures. Upon seeding, neurons slowly adhered to the PDL-coated surface, particularly to the bottom of the nodes, and excess cells on top of the microstructures were aspirated [93]. For the two-compartment microfluidic system, cells were seeded in the somal compartment of the μEFs [94].

All cultures were maintained in a humidified incubator at 37ºC with 5% CO_2, and half-medium change was performed weekly .

4.3.4. Electrophysiology recordings

Extracellular electrical activity from neuronal cultures was recorded by placing each MEA into the headstage of the MEA2100 system (Multi Channel Systems MCS GmbH, Reutlingen, Germany). Signal are amplified and digitized directly on the headstage, and various headstage types are available to accommodate different electrode layouts, including 60- and 256-electrode MEAs. The MEA2100-Mini system (Multi Channel Systems MCS GmbH, Reutlingen, Germany) is a miniaturized recording system designed for 60- and 120-electrode MEAs. The interface board (IFB-C) receives data from up to two headstages (1-4 MEAs) and connects to the computer via USB 3.0 SuperSpeed port. The Multi Channel Experimenter (Multi Channel Systems MCS GmbH, Reutlingen, Germany) software provides an interface for acquisition, real-time visualization and online analysis of neuronal data. The program allows to design experiments by combining virtual instruments (*e.g.*, recorder, filter, spike detector) in a workbench-like environment, and export the recorded data for posterior offline analysis.

Electrophysiology experiments were conducted at 37ºC with 5% CO_2. Cultures were allowed to settle in the headstage before each recording session.

Multi-node networks

Electrophysiological recordings were obtained at 13 days *in vitro* (DIV) with a sampling rate of 10 kHz. Spontaneous activity was recorded for 2 min followed by single node stimulation. A sequence of 5 to 10 biphasic voltage pulses (−500/500 mV, 200 μs per phase) was delivered to each node independently, allowing to return to baseline activity levels between stimuli [93].

Raw data was provided by Forró *et al.* [93], and further analysed offline in MATLAB. Signals were band-pass filtered (3rd order acausal Butterworth filter, 200-3000 Hz) and neuronal spikes were detected using an amplitude threshold method based on the standard deviation of the background noise [96]. Concisely, neuronal signals can be described by a mixture of a normally distributed noise component (ranging from 2 to 10 μV) and a spike component featuring sparsely distributed, large amplitude neuronal spikes (ranging from 0.02 to 0.4 mV) [97]. Thus, an amplitude threshold based on the background noise levels allows to identify neuronal spikes as outliers in neuronal signals. For Gaussian noise, the median absolute deviation, MAD, of the signal is equal to 0.6745σ, where σ is the standard deviation of the Gaussian noise [98]. Therefore, the threshold, Thr, for each electrode was defined as follows,

$$Thr = n \times \sigma_n, \qquad \sigma_n = \frac{MAD}{0.6745} = median\left\{\frac{|x|}{0.6745}\right\}, \qquad [16]$$

where x represents the filtered signal, σ_n is an estimate of the standard deviation of the background noise and n is a multiplier factor for the standard deviation, typically between 3 and 5 ($n = 4$). Median-based estimators provide a more robust method against outliers (*i.e.*, neuronal spikes) with respect to the regular standard deviation of the signal, assuming that spikes account for a small fraction of the signal. Spike time were extracted at the threshold-crossing point, and any spikes occurring within the following **2** ms were discarded (dead time). Neurons are unable to fire two consecutive action potential within a 2 to 3 ms window due to the refractory period; thus, by imposing a minimum interspike interval, biphasic and triphasic action potential are not detected more than once. For each spike, the maximum absolute voltage was extracted within a limited window of **2** ms, related to the duration of a single spike. This step is particularly relevant for the subsequent analysis where the precise timing between events is required.

Highly synchronized activity of neurons within nodes is expected during bursts, which may complicate the spike detection task since spikes appear overlapped. Since recordings are not long, excluding these periods was discarded. A more conservative approach was adopted, detecting only negative spikes and further decreasing the dead time to 1 ms, assuming that subsequent correlation computation will keep only the relevant information.

Two-compartment microfluidic system

Electrophysiology experiments were conducted at 18 DIV with a sampling rate of 10 kHz. Spontaneous activity recordings were obtained using the Multi Channel Experimenter software. The digital signal processor (DSP) integrated in the interface board was configured in the Experimenter software: signals were high-pass filtered (2nd order causal Butterworth filter, 200 Hz) and neuronal spikes were detected in real-time using an amplitude threshold set to ± 6 times the standard deviation of the noise with a dead time of 2 ms.

Spike train data was exported, and further analysed offline in MATLAB. Network burst activity was excluded from the analysis since overlapping spikes may difficult challenge the detection task due to high firing rate observed during burst precise timing is important. Burst periods were excluded since spike detection suffers from confounding factors and the precise spike time is difficult to obtain [94]. The network instantaneous firing rate was computed by convolving the spike train of each electrode with a Gaussian kernel with a standard deviation of 10 ms and averaging across electrodes [99]. A Gaussian kernel allowed to obtain a smooth estimation of the firing rate of the network, which contrasts with estimates using rectangular windows. Network bursts were detected when the firing rate exceeded a threshold of **5** Hz, and excluded from the subsequent analysis.

Real-time analysis

The main goal of this implementation is to update the connectivity information from a neuronal culture coupled to a microelectrode array as new spike events are detected, and provide this information in “real-time” to the user in an informative and intuitive way.

The connection between the MEA2100(-Mini) system and MATLAB was established using the McsUsbNet dynamic link library (DLL) from Multi Channel Systems (https://github.com/multichannelsystems/McsUsbNet).

Electrophysiology experiments were performed at 2-3 weeks *in vitro* with a sampling rate of 10 kHz. Raw signals were high-pass filtered (2nd order causal Butterworth filter, 200 Hz) by the analog filter circuit integrated in the headstage, and then transferred to MATLAB. The raw data stream was received in 500 ms batches containing 5000 sample points per electrode, as they were available. For each batch, neuronal spikes were identified as negative peaks below an amplitude threshold of 5 times the standard deviation of the signal with a dead time of 2 ms. Similarly, bursting periods were excluded since overlapping action potentials may difficult the spike detection task. The network instantaneous firing rate was obtained by convolving the spike train of each electrode with a half-Gaussian kernel with a standard deviation of 10 ms and averaging across electrodes. The half-Gaussian kernel essentially refers to the right half of the normal

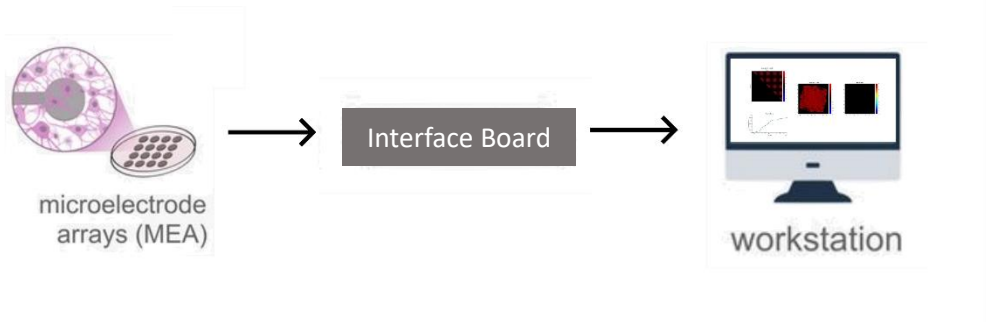

Figure IV-3. General pipeline developed for the analysis of real experimental data in "real-time". Electrophysiological activity is recorded via microelectrode arrays, and transferred to a workstation in "real-time". The data is processed by a connectivity inference algorithm, and the connectivity matrix and corresponding map is displayed for the user. Adapted from [17].

distribution. In contrast to a normal distribution, this kernel only considers spikes that already fired for the computation of the mean instantaneous firing rate – causal window –, allowing to provide a value in real-time [100]. When the firing rate exceeded a defined threshold, spikes were discarded from the subsequent analysis. For each batch, the connectivity inference algorithm was executed independently for each single events, and the connectivity information was presented summarizing the results after each batch was processed.

Spike train data was exported for posterior offline analysis in MATLAB.

Chapter V

Results and discussion

5.1 Synthetic spike train data

Synthetic spike train data was generated in MATLAB to determine the underlying distribution of the time intervals between pairs of spikes from two independently firing units. Subsequently, the theoretical distribution under the null hypothesis of no dependence between firing units was used as the reference distribution to detect and further characterize statistically significant connections.

Let $({t_X}^n)_{n=1}^{N_X}$ denote a finite sequence of spike times from a given firing unit X, where the index n indicates the nth spike of the sequence and N_X is the total number of spikes. Stated a reference unit R and a target unit T, the corresponding spike trains $\left({t_R}^i\right)_{i=1}^{N_R}$ and $\left({t_T}^j\right)_{j=1}^{N_T}$ were generated by two independent Poisson point processes with mean interarrival times τ_R and τ_T, respectively. Given a reference spike at time ${t_R}^i$ and a target spike at time ${t_T}^j$, the time interval between spikes τ_{ij} was defined as,

$$\tau_{ij} = {t_T}^j - {t_R}^i, \quad \forall i \in \{1, \dots, N_R\}, j \in \{1, \dots, N_T\} \qquad [17]$$

If the reference spike temporally precedes the target spike, the time interval between spikes τ_{ij} is positive; otherwise, it is negative. Considering all possible pairs of spike times $({t_R}^i, {t_T}^j)$ with the first element drawn from the reference train and the second element from the target train, it follows that the total number of time intervals is given by $N_R N_T$.

In the subsequent analysis, the mean interarrival time was set to 100 ms ($\tau_R = \tau_T$), and three different values of the total number of spikes were considered: 100, 1000 and 10000 ($N_R = N_T$). The time intervals between pairs of spikes τ_{ij} were binned into a histogram with a bin width h of 1 ms and a causality window τ_c set to ±50 ms. The causality window τ_c defines the range of time

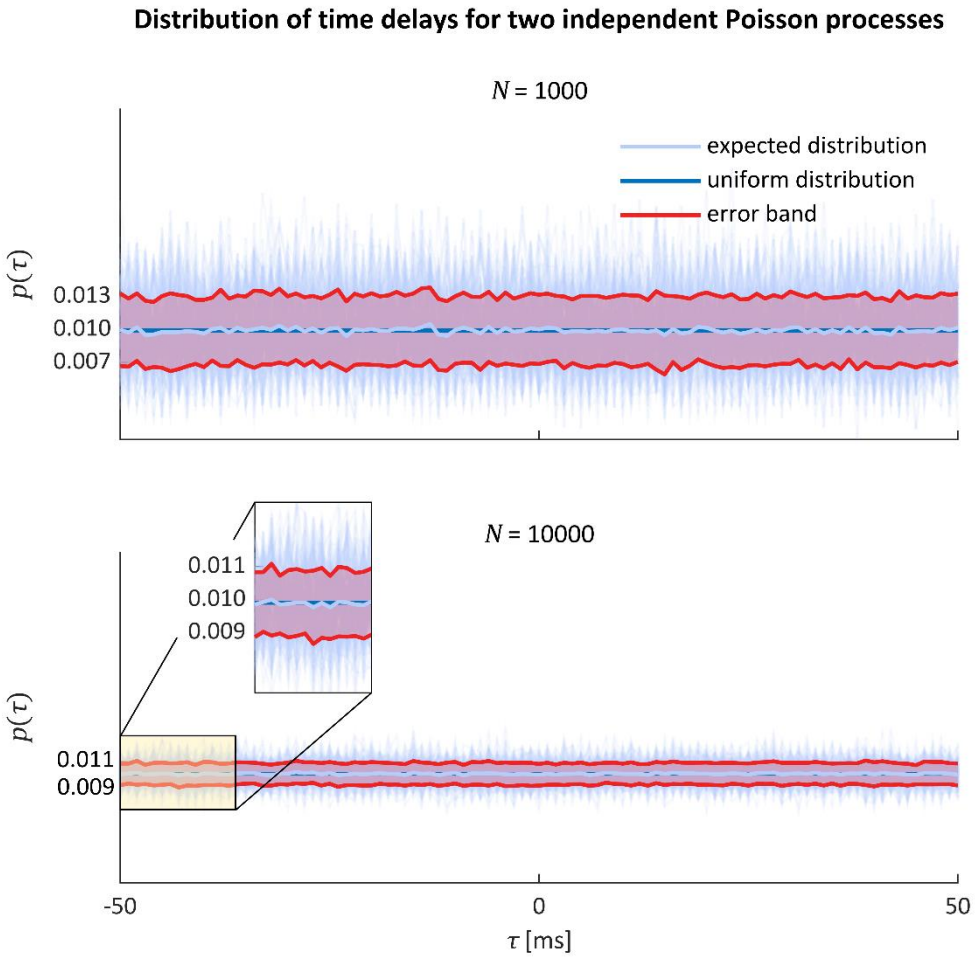

Figure V-1. Distribution of time delays for two independent Poisson processes. The distributions of time delays between events for two independent Poisson processes with 1000 (top panel) and 10000 (bottom panel) events were obtained. The probability density functions estimated in each trial (T = 200) are represented in light blue (transparency). The light blue curve corresponds to the mean value of the probability density function in each bin; the red curves define the error band by considering values wthin 1 standard deviation from the mean value (n = 1). The theoretical uniform distribution is shown in dark blue.

intervals represented in the histogram. Each histogram bin value was then normalized by the total number of time intervals within the causality window n_c and the bin width h such that the total area of the histogram was equal to 1. The density histogram provides an estimate of the probability density function that is independent of the total number of observations and the bin width, and thereby useful to compare distributions of a given variable [101].

The law of large numbers states that, as the number of trials increases, the sample mean converges to the expected value [102]. The expected distribution of time intervals (light blue curve in **Figure V-1**) was estimated by generating independent Poisson processes over multiple trials and averaging the obtained distributions (transparent light blue curves in **Figure V-1**). For each value of N_R, the above procedure was repeated 200 times. The mean density value, μ_k, and the

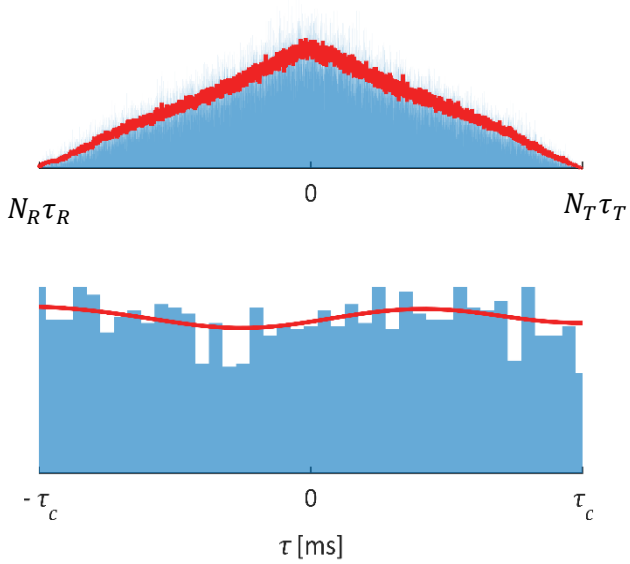

Figure V-2. Distribution of time delays for two independent Poisson processes. The distribution of time delays between events for two independent Poisson processes are represented without considering any causality window in the top panel. The red curve refers to the probability density function. The bottom panel present the same distribution within a causality window $\pm\tau_c$.

corresponding standard deviation, σ_k, were calculated for each bin k, and an error band was defined as $\mu_k \pm n \cdot \sigma_k$, where n is an integer. The time intervals approximately follow a uniform distribution (dark blue curve in **Figure V-1**) within the causality window and, therefore, there is no preferred time interval between events from independent units, as expected. The selected number of trials ($T = 200$) allowed to obtain an estimate of the probability density function with a RMSE below 0.001, with respect to the theoretical uniform distribution.

The above results show a dependence between the number of events, N, and the standard deviation, σ. The width of the error band is reduced by a factor of 3 when the number of events, N, increases from $N = 1000$ to $N = 10000$.

The closed-form expression for the standard deviation, σ, was derived for two independent Poisson point processes. The distribution of time intervals, τ, for two independent Poisson processes is shown for an arbitrary set of parameters ($N_R\tau_R = N_T\tau_T$, considering the same recording time for each unit) is obtained (**Figure V-2**). The total area under the curve for any probability density function is equal to 1. Therefore, the intersection with the *y*-axis, b, and the slope, m, can be expressed as,

$$N_R\tau_R \cdot b = 1 \Leftrightarrow b = \frac{1}{N_R\tau_R} = \frac{1}{N_T\tau_T} \quad [18]$$

$$m = \frac{b}{N_R\tau_R} \Leftrightarrow m = \frac{1}{N_R\tau_R \cdot N_R\tau_R} \quad [19]$$

For $\tau \in [-\tau_c, \tau_c]$ and $\tau_c \ll N_R\tau_R \cdot N_T\tau_T$, the probability density function, $p(\tau)$, is given by,

$$p(\tau) = \begin{cases} \frac{1}{N_R\tau_R \cdot N_R\tau_R}\tau + \frac{1}{N_R\tau_R}, & \tau \in [-\tau_c, 0] \\ \frac{1}{N_R\tau_R}, & \tau \in [0, \tau_c] \end{cases} \quad [20]$$

$$\Leftrightarrow p(\tau) \approx \frac{1}{N_R\tau_R}, \qquad \tau \in [-\tau_c, \tau_c]. \quad [21]$$

The time intervals approximately follow a uniform distribution within the causality window.

The number of time intervals, τ, represented within the causality window, n_c, can be calculated as the probability of a given time delay belonging to the causality window, $P(\tau \in [-\tau_c, \tau_c])$, multiplied by the total number of possible delays, $N_R N_T$,

$$P(\tau \in [-\tau_c, \tau_c]) = p(\tau) \cdot H = \frac{1}{N_R\tau_R} \cdot 2\tau_c \Leftrightarrow P(\tau \in [-\tau_c, \tau_c]) = \frac{2\tau_c}{N_R\tau_R} \quad [21]$$

$$n_c = P(\tau \in [-\tau_c, \tau_c]) \cdot N_R N_T \Leftrightarrow n_c = \frac{2\tau_c}{N_R N_T} \cdot N_R N_T \Leftrightarrow E_{\tau_c} = 2\tau_c \frac{N_R}{\tau_T} = 2\tau_c \frac{N_T}{\tau_R}. \quad [22]$$

Focusing the attention on the causality window, a new probability density function, $\tilde{p}(\tau)$, can be defined within its limits. Since the distribution of delays is approximately uniform,

$$\tilde{p}(\tau) = \frac{1}{2\tau_c}. \quad [23]$$

The number of events within a single bin can be obtained as,

$$\tilde{P}(\tau \in [0, h]) = \frac{1}{2\tau_c} \cdot h \Leftrightarrow \tilde{P}(\tau \in [0, h]) = \frac{h}{2\tau_c} \quad [24]$$

$$n_h = \tilde{P}(\tau \in [0, h]) \cdot n_c \Leftrightarrow n_c = \frac{h}{2\tau_c} \cdot 2\tau_c \frac{N_R}{\tau_T} \Leftrightarrow E_h = h\frac{N_R}{\tau_T} = h\frac{N_T}{\tau_R}. \quad [25]$$

The error related to each bin count is equal to the square root of the respective count. By normalizing these values by the total number of counts within the causality window and the bin size,

$$\tilde{p}(\tau) = \frac{n_h \pm \sqrt{n_h}}{n_c h} \Leftrightarrow \tilde{p}(\tau) = \frac{1}{2\tau_c} \pm \frac{\sqrt{h\frac{N_R}{\tau_T}}}{2\tau_c \frac{N_R}{\tau_T} h} \Leftrightarrow \tilde{p}(\tau) = \frac{1}{2\tau_c} \pm \frac{1}{2\tau_c}\sqrt{\frac{\tau_T}{N_R h}}. \quad [26]$$

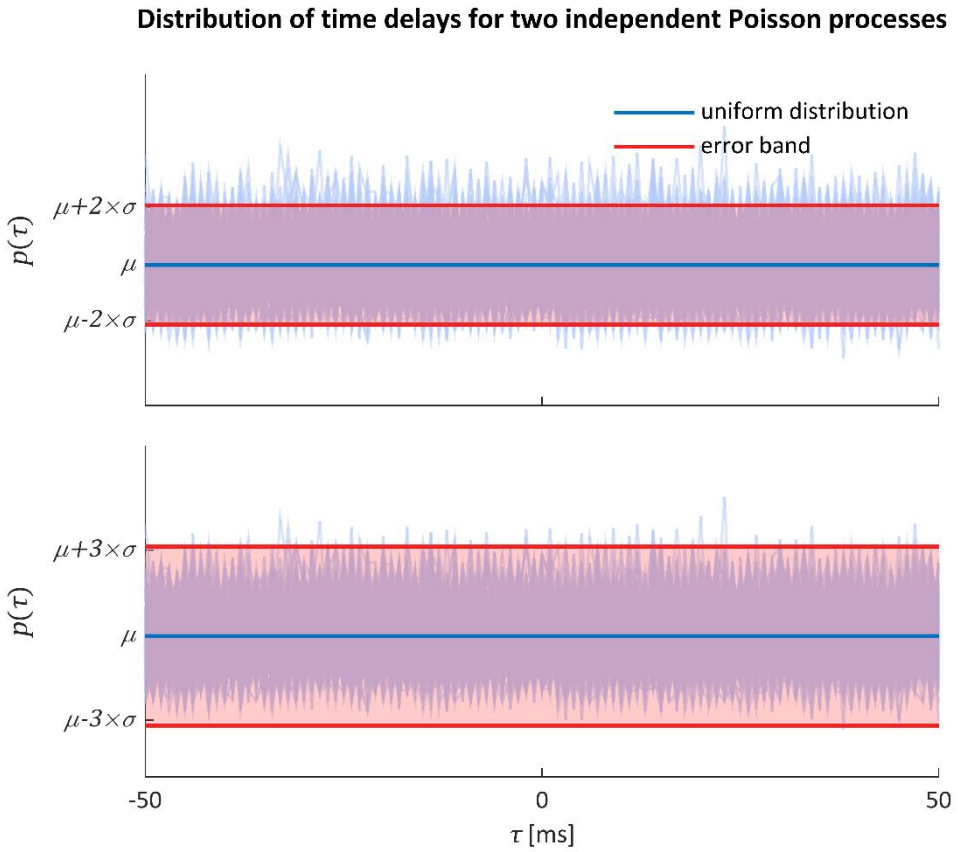

Figure V-3. Error band for the distribution of time delays for two independent Poisson processes. For the same distribution, by considering different number of standard deviations ($n = 2$ and $n = 3$, respectively), different percentages of data are included within the error band.

These results confirm that the distribution of time delays for two independent Poisson processes is approximately a uniform distribution, with a standard deviation that can be expressed as a function of the causality window, the bin width, and the parameters used to generate the Poisson processes. Therefore, the uniform distribution can be used as a reference to detect functional connections between units, where an "accumulation of area" at the corresponding latency is expected.

A larger causality window implies that more datapoints are represented in the histogram; thereby, the error associated with the distribution decreases. Regarding the bin width, a larger bin smooths the histogram and, as a result, the final distribution converges to the expected distribution, decreasing the error associated with each bin count. The ratio between number of events and the mean interarrival time for distinct units affects the standard deviation since a larger number of events or a smaller interarrival time both contribute with more counts within the causality window, decreasing the error band width.

In experimental setups, when assessing the confidence of the connection between two neuronal units, deviations from the baseline can be discarded if they are located within the error band. In

this case, where the mean inter-spike interval and the number of spikes is not defined by the user, but depends on the nature of neuronal cultures, the number of time delays detected within the causality window can be used to estimate the error band,

$$e = \frac{1}{2\tau_c}\sqrt{\frac{\tau_T}{N_R h}} \Leftrightarrow e = \frac{1}{2\tau_c\sqrt{h}}\sqrt{\frac{\tau_T}{2\tau_c N_R}}\sqrt{2\tau_c} \Leftrightarrow e = \frac{1}{\sqrt{2\tau_c h}}\sqrt{\frac{1}{n_c}}.$$

$$\Leftrightarrow e = \frac{1}{\sqrt{2\tau_c h n_c}} \quad [27]$$

By establishing an error band considering n standard deviations from the uniform distribution, deviations from this reference function can be assessed and used to quantify functional connections. Depending on the number of standard deviations considered, connections can be detected as outliers.

5.2 New algorithm

A novel algorithm based on the pairwise cross-correlation for connectivity inference from neuronal data is herein proposed. Besides providing a full characterization of the interactions between neuronal units, including confidence of connection, latency and direction, an online approach is proposed, allowing to update the connectivity matrix as new events are detected. This information is summarized in a connectivity matrix and the corresponding delay matrix.

For simplicity, the algorithm is detailed for two units, but the analysis can be generalized to any number of units since the pipeline is based on pairwise comparisons.

Online approach

Let a spike event, E, be represented by its occurrence time, t_s, and the unit which fired it, n_s. The pseudocode describes the sequence of steps performed to handle a stream of events and generate the cross-correlation histogram for a given pair of units i and j.

Algorithm 1. Compute the cross-correlation histogram for a given pair of units i and j

---

```
ref    ← i
target ← j
IF new_event_detected
        IF n_s equals ref
                lag ← buffer( target ) – t_s
        ELSE
                lag ← t_s – buffer( ref )
        END IF
        bin          ← convert_from_ms_to_samples( lag )
        CCH( bin ) ← CCH( bin ) + 1
END IF
```

Upon the firing of a spike event E at time t_s by unit $n_s = i$, the connections between i and all other units are assessed pairwise. For a given pair of units, the connection is assessed one time since the histogram is symmetric and contains information about interactions in both directions, depending on whether we consider a positive or a negative delay. Therefore, we start by defining the reference unit and the target unit, and the cross-correlation histogram is obtained accordingly. A positive delay indicates that events in the reference unit precede activity in the target unit; the opposite is true for a negative delay.

The corresponding timestamp, t_s, from unit n_s, is then compared to previous spike events fired by the other unit. A buffer is used to store these past events. Since we assume that causal events take place inside a chosen time window, the buffer needs to be continuously updated. This ensures that the maximum lag between any stored event and the current time is within the causality window.

The time delay is computed as the difference between a target and a reference spike. When a spike event is detected for a given unit, the buffer referring to the other unit may contain more than one event. In these cases, this operation is performed for each pair of reference and target spikes, and an array with time delays is obtained. These intervals are converted to the corresponding bin in the cross-correlation histogram, and the new information is added to the histogram.

To generate the cross-correlation histogram, the bin size and the causality window are defined as parameters of the algorithm. The choice of the bin size can significantly affect the shape of the histogram: narrow bins usually lead to noisy distributions with irrelevant information whereas wider bins may hide important details. Regarding the causality window, the biophysical properties

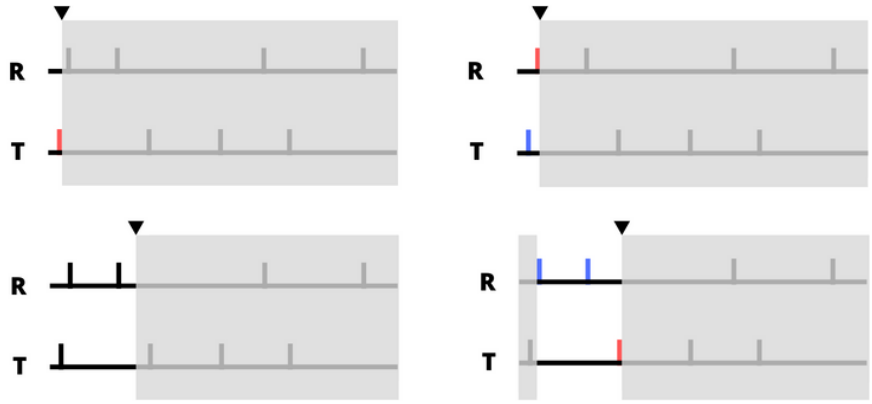

Figure V-4. How does the algorithm deal with a stream of incoming spike events? The grey background represents data to which the algorithm does not have access. When a new event (in red) is detected in one unit, the algorithm only has access to past events within the causality window (white background). The black marker indicates the current time and the left border of the causality window. Each detected event is compared with past events from the other unit (in blue).

of neurons should be taken into account to select a reasonable time interval (10 ms) within which causal events are expected to occur.

How to characterize connections?

From the cross-correlation histogram, the weight and time delay for the connection between *i* and *j* can be extracted by converting the cross-correlation histogram into the corresponding probability density function. This normalization allows to compare the resulting distribution with the expected uniform distribution when no link between units is found.

A filtering operation is first applied to the histogram to reduce the effect of spurious random connections. Here, a gaussian kernel with a standard deviation equal to the bin size is adopted. To avoid boundary effects as a result of the convolution operation, a wider window is considered to obtain the cross-correlation histogram and perform the smoothing. For the subsequent steps, only the bins within the causality window are kept.

After obtaining the probability density function, the goal is to measure how different this distribution is from the normalized uniform distribution. The total area under a density curve is equal to 1. When two probability density functions referring to the same continuous random variable are superimposed, the sum of all the individual areas between the curves, A, is equal to 0. For a pair of units (i, j), if each one of these patches is represented by a_{ij}^n, this can be expressed as,

$$A = \sum_n a_{ij}^n = 0 \qquad [28]$$

where n is the total number of patches. Additionally, a variable s_{ij}^n can be defined to distinguish between an area a_{ij}^n above the uniform distribution, with $s_{ij}^n = 1$, and under this curve, where $s_{ij}^n = -1$.

When a causal relationship between a pair of units (i, j) exists, a significant deviation from the background is observed in the corresponding probability density function, outside the error band defined based on the number of counts in the cross-correlation histogram. These isolated and high-amplitude features contrast with the randomness of the connections represented in the flat background. Depending on whether a peak or trough is present, we can then classify these interactions as excitatory or inhibitory.

To obtain the weight for the connection between *i* and *j*, patches outside the error band are found based on the baseline level of the estimated distribution. The baseline level corresponds to the distribution of random intervals between events. If the baseline level is above the theoretical probability density function, only negative areas are considered – inhibitory connection; otherwise, only positive areas are considered – excitatory connection. The confidence, c_{ij}, is given by the ratio between the largest of these areas, a_{ij}^N, and the total area considering the patches n such that $s_{ij}^n = s_{ij}^N$,

$$c_{ij} = \begin{cases} \dfrac{a_{ij}^N}{\sum_n \dfrac{s_{ij}^n + 1}{2} a_{ij}^n}, if\ s_{ij}^N = 1 \\ \dfrac{a_{ij}^N}{\sum_n \dfrac{s_{ij}^n - 1}{2} a_{ij}^n}, if\ s_{ij}^N = -1 \end{cases} . \quad [29]$$

The time delay assigned to the connection, d_{ij}, is calculated as the lag corresponding to the highest absolute value within the range covered by a_{ij}^N.

Finally, the computed weight and time delay is assigned to the corresponding entry in the connectivity matrix and delay matrix, respectively.

5.3 NEURON simulations

The algorithm presented in the previous section was validated with synthetic spike train data generated by a simple computational neuronal model featuring two neurons simulated in NEURON. The results are shown according to the type of interaction between neurons.

Independent units

Two independent units were simulated, and the corresponding cross-correlation histogram was obtained. Although the algorithm had access to the whole recording, individual spikes were provided at a time to simulate a real-time application. Following a gaussian filtering to remove spurious connections, the probability density function was estimated, along with the corresponding error band. As expected, the probability density function approximately follows a uniform distribution, with no preferred time interval between events fired by both units (**Figure V-5**). Spike trains with different firing rates were simulated, and the same trend in the estimated probability density function was observed considering the total simulation time (5 min in the case of independent units).

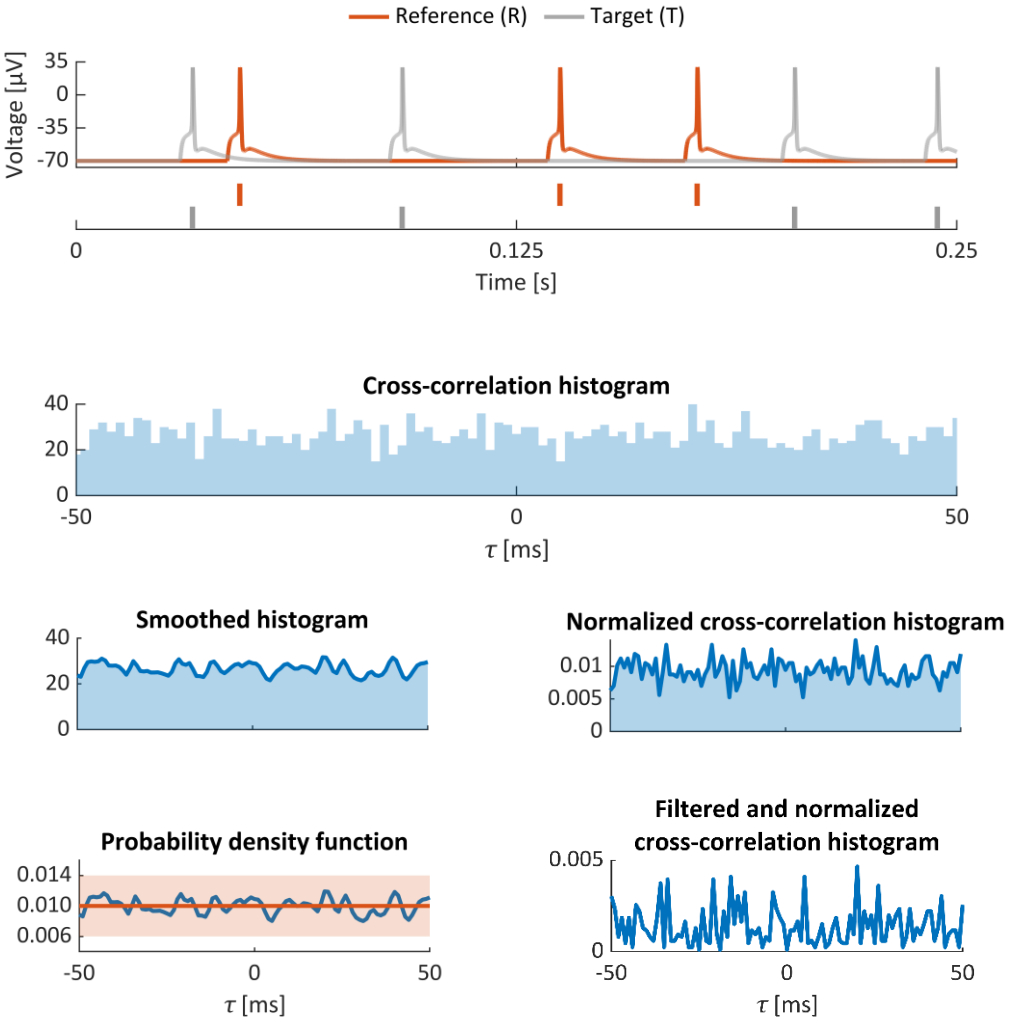

Figure V-5. Analysis of spike train data from two independent neurons. The voltage traces and raster plot generated by both neurons is presented above, followed by the corresponding cross-correlation histogram. The bottom four panels show the steps to obtain the final probability density function (left) and the filtered and normalized cross-correlation histogram proposed in [66].

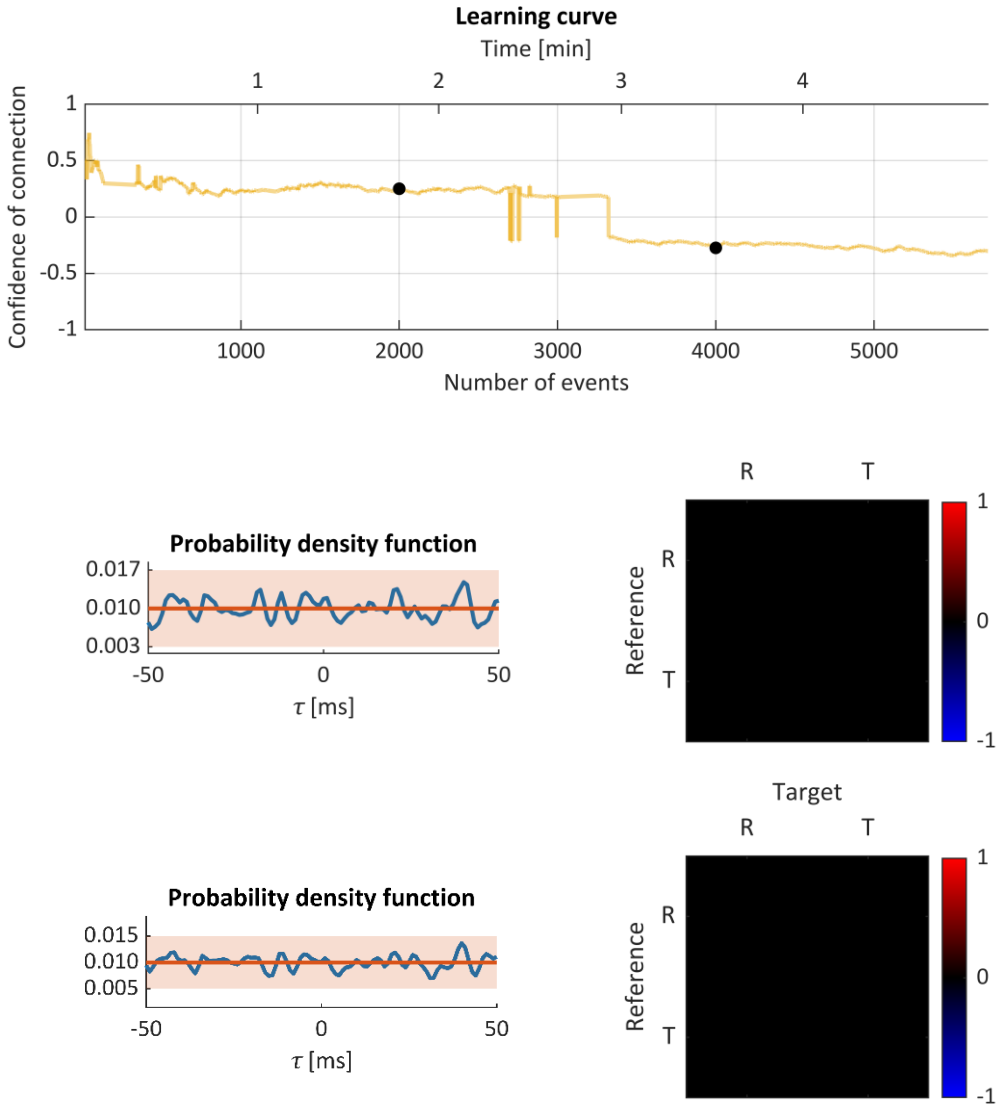

Figure V-6. Learning curve for two independent neurons. The black markers in the learning curve correspond to the pairs of estimated probability density function and connectivity matrix displayed below.

Considering an error band equal to two standard deviations from the uniform distribution, no connection was found. In order to understand how the confidence of connection value evolves as the number of detected events increases, and highlight the relevance of considering an error band to distinguish between significant and non-significant connections, the largest area between the obtained distribution and the reference uniform distribution was computed, even when no outliers outside the error band were identified for illustrative effects – learning curve (**Figure V-6**). The confidence of connection assumed both positive and negative values within a limited range. When no dependence exists, the areas around the uniform distribution will be similar; thus, both positive and negative values are valid. The error band ultimately allows to discard noisy connections, with

no connections represented in the connectivity matrix. As the number of events increases, the width of the error band also decreases, as already anticipated.

Excitatory connections

The same procedure was repeated for two positively correlated neurons, considering different synaptic weights for the simulation. Again, the firing rate for both neurons was varied, considering the same value for both units, and a ratio of 10 and 0.1 between the firing rate of the reference neuron with respect to the target neuron.

Considering again an error band equivalent to two standard deviations, the obtained distribution considerably differs from the uniform distribution. The convergence to the final value of confidence of connection is not immediate. As the number of detected events increases, the corresponding probability density function approximates its final shape and, consequently, so does the confidence of connection. Also, the increasing number of counts represented in the histogram results in a decrease of the width of the error band, as already mentioned for the previous case of independent units. The synaptic delay represented in the connectivity matrix is around the value defined in the simulation (2 ms).

For the same synaptic weight, an increase in the frequency rate of the target neuron is not expected to result in a faster convergence of the confidence value. Even though for the same amount of time, a larger number of events are detected in this situation, such increase is due to spikes fired by the target neuron, which are not expected to have an influence on the reference neuron. Therefore, in this situation the time for the convergence will be similar to the one observed when the two firing units present a similar firing rate (first and second panels in **Figure V-8**). On the other hand, if the firing rate of the reference neuron increases, the larger number of spikes are expected to trigger a response in the target neuron more regularly, and thus less time will be required for the value of the confidence of connection to converge. Thus, the rate of convergence will depend on the number of spikes fired by the reference neuron. In this case, a very high firing rate was tested (100 Hz) for the reference neuron (third panel in **Figure V-8**). Although the synaptic weight was kept the same, the confidence of connection converges to a higher value, almost reaching a value of 1. A possible explanation for this unexpected behaviour is that the higher firing rate of the reference unit maintains the baseline membrane potential of the target unit closer to the threshold. For this reason, even if the synaptic weight is lower than the minimum value that consistently triggers activity in a target neuron, the target neuron will require a lower synaptic weight to be triggered. Finally, if we consider a higher value for the synaptic weight in the simulation, the reference neuron will be capable of consistently triggering a response in the target neuron upon each firing event. Since more pairs of related spikes will be identified, the

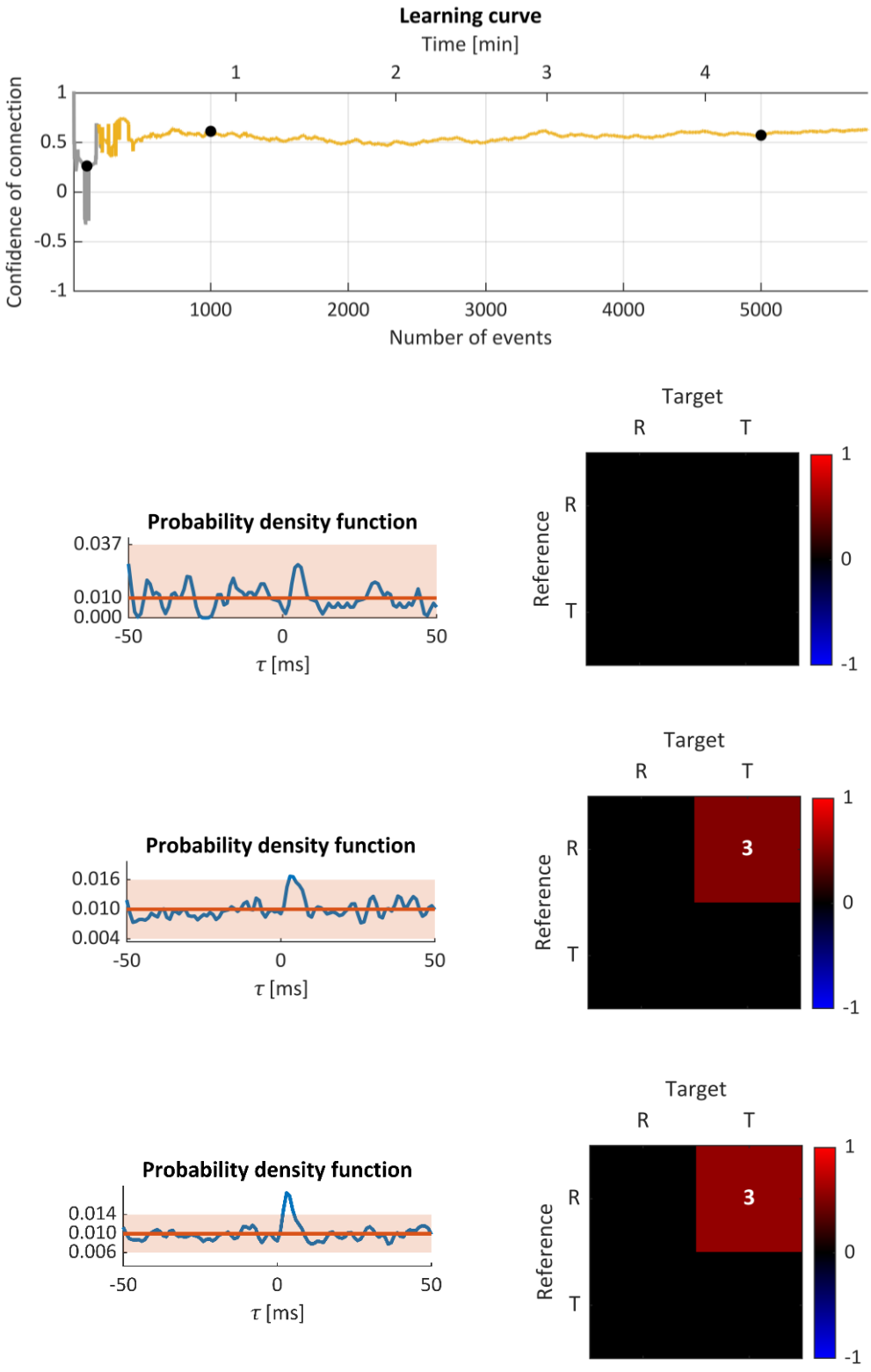

Figure V-7. Learning curve for an excitatory connection. The black markers in the learning curve correspond to the pairs of probability density function and connectivity matrix displayed below.

convergence to the final value of the connection will be faster when compared to cases with lower values for the synaptic weight (forth panel in **Figure V-8**).

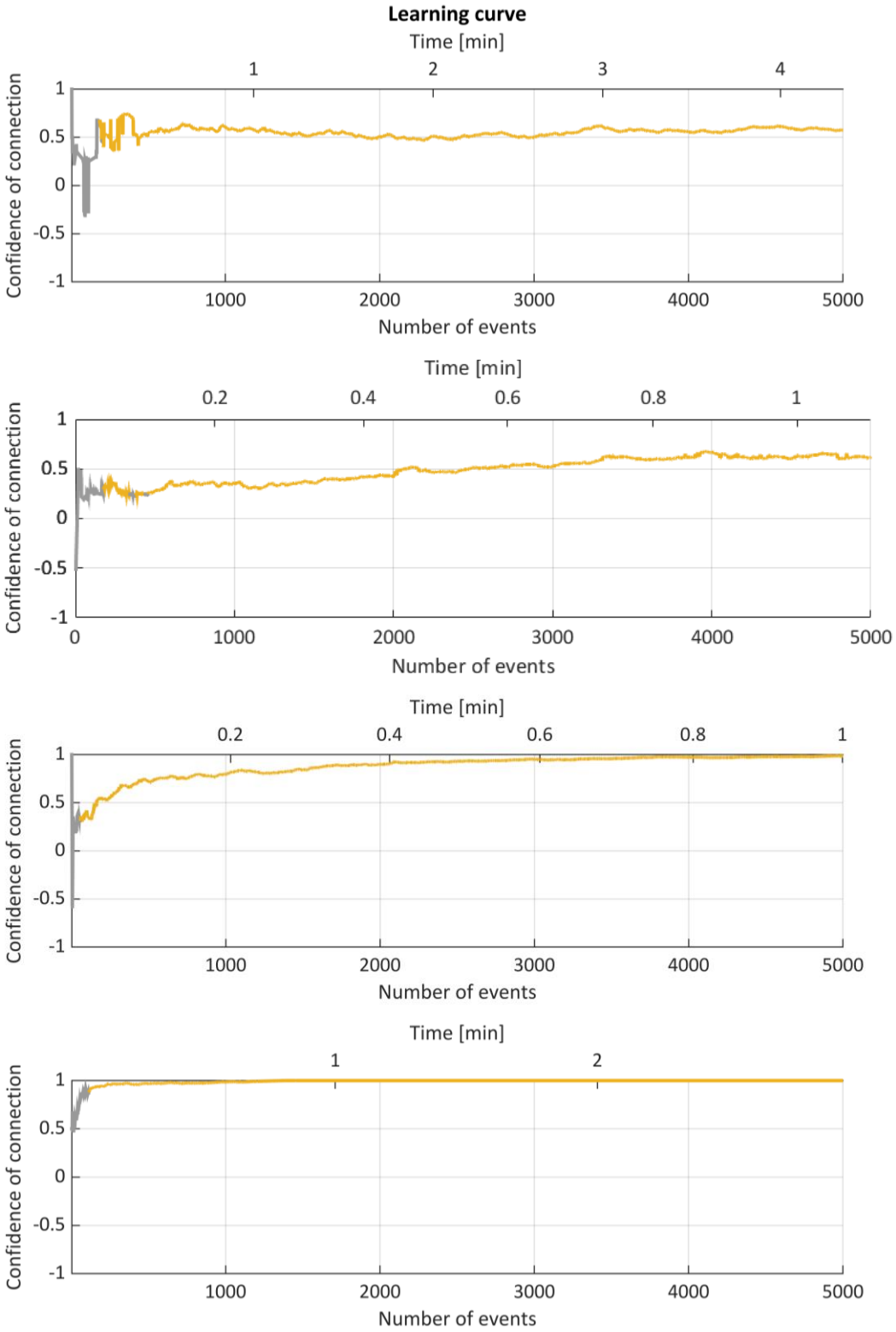

Figure V-8. Learning curve for different excitatory connections. The first curve corresponds to a synaptic connection with synaptic weight of 0.005, and a similar firing rate (10 Hz) for both neurons. The second and third curves refer to the same synaptic weight of 0.005, but with a higher firing rate for the target and reference neurons, respectively. The last curve corresponds to a similar case to the first one, but with a synaptic weight of 0.008.

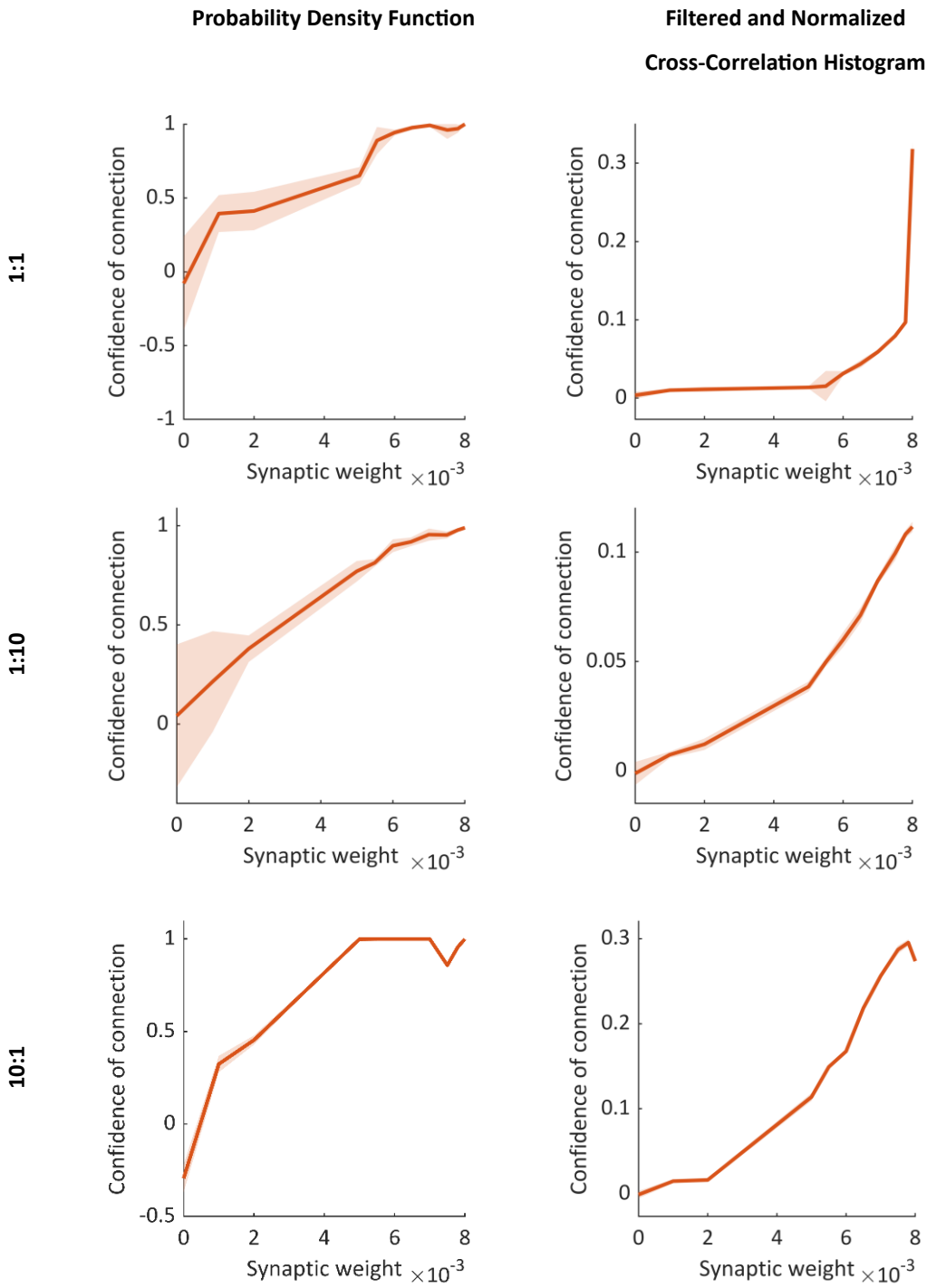

Figure V-9. Confidence of connection as a function of the synaptic weight defined for neuronal simulation considering different firing rates for the neurons and different algorithms for connectivity inference in excitatory connections. In left column, the results are presented for the proposed algorithm based on the probability density function, whereas the right column refers to the results obtained from the filtered and normalized cross-correlation histogram. The ratios depicted correspond to the ratio between firing rate of the reference neurons and the firing rate of the target neuron. Regarding each row, neurons were considered with the same firing rate, a 10x higher firing rate for the target neuron, and a 10x higher firing rate for the reference neuron, respectively. For each synaptic weight, 5 simulations were conducted, and the mean and standard deviation (error bar) are presented.

Besides implementing a new approach for the detection of connections, the algorithm proposed in [66] was also tested with synthetic data. As already mentioned in Chapter III, this algorithm is based on the computation of the filtered and normalized cross-correlation histogram, and subsequent detection of the largest peak as a putative functional connection. The main issue with this approach is the need for a subsequent step of thresholding to remove non-significant connections. The thresholding method is based on the assumption that functional connections are sparse in neuronal networks and most of the putative detected connections are not real connections. Thus, the mean of the strength of connections and the corresponding standard deviation are computed and used to remove those non-significant connections. However, if one is interested in assessing the characteristics of a connection without having information about others, such approach cannot be used. Therefore, the proposed methodology provides means to detect relevant connections without having to establish any comparison with other connections. Another issue is the dependence of the approach based on the filtered and normalized cross-correlation histogram on the levels of activity. Even if the firing units present different firing rates, if a value for the synaptic weight is defined for the simulation, the resulting confidence of connection should have the same value, regardless of the firing conditions. The approach based on the probability density function allows to obtain estimates in line with this. On the other hand, the range for the weight of connection extracted from the filtered and normalized cross-correlation histogram varies with the activity level of the firing units (**Figure V-9**).

Inhibitory connections

The same procedure was repeated for two neurons connected by an inhibitory synapse, considering different synaptic weights for the simulation.

Considering again an error band equivalent to two standard deviations, the obtained distribution considerably deviates from the uniform distribution. As the number of detected events increases, the corresponding probability density function approximates to its final shape and, once again, the width of the error band decreases. The synaptic delay represented in the connectivity matrix significantly differs from the value defined in the simulation (2 ms). This could be due to the fact that inhibitory interactions have a larger decay and, thus, its effect is observed during a larger time window. Therefore, when compared to the detection of excitatory connections, the area outside the error band comprises a wider interval of time delays (**Figure V-10**). Consequently, the choice of the causality window, especially for the inhibitory connections, should consider a larger enough range so that the deviation from the baseline level is readily distinguished from the baseline level given by the random time intervals between spikes. In this case, the causality window was set to ±50 ms, even if synaptic delays are typically shorter in time [31].

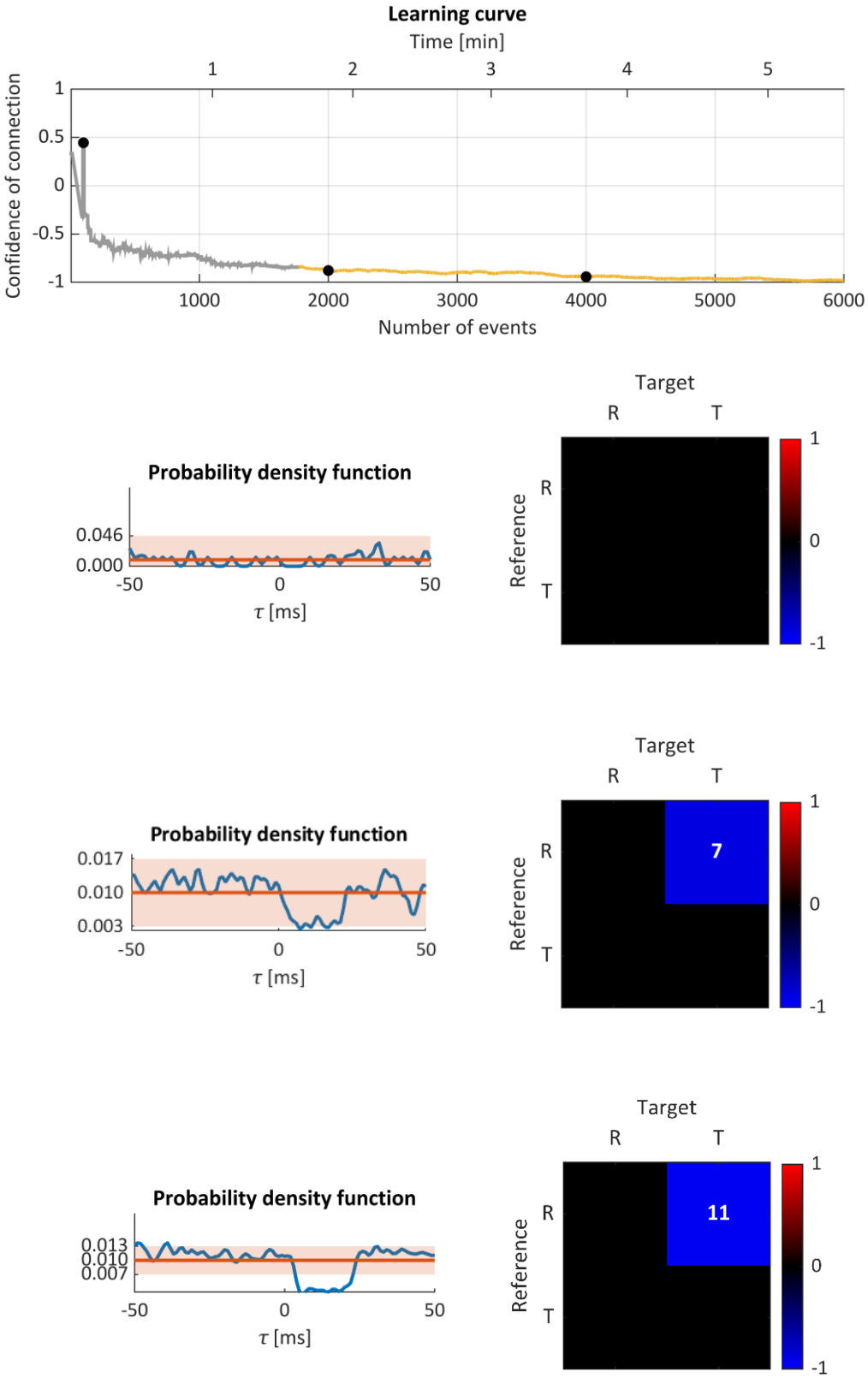

Figure V-10. Learning curve for an inhibitory connection. The black markers in the learning curve correspond to the pairs of probability density function and connectivity matrix displayed below.

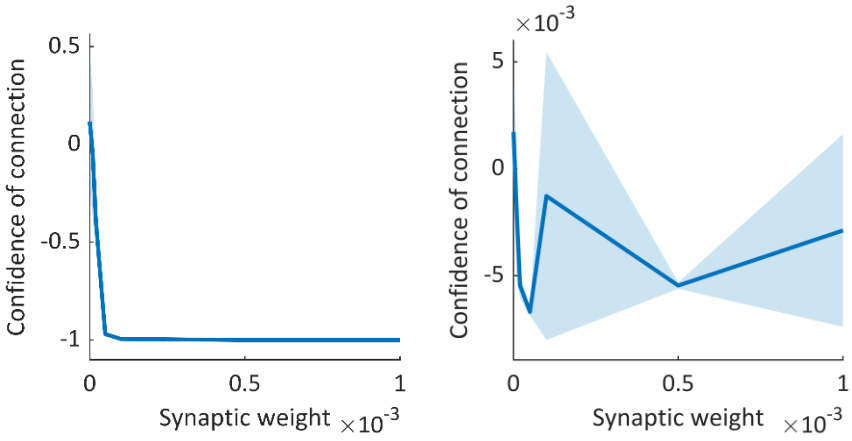

Figure V-11. Confidence of connection as a function of the synaptic weight defined for neuronal simulation considering different algorithms for connectivity inference in inhibitory connections. On the left, the results are presented for the proposed algorithm based on the probability density function, whereas the right curve refers to the results obtained from the filtered and normalized cross-correlation histogram. For each synaptic weight, 5 simulations were conducted, and the mean and standard deviation (error bar) are presented.

Similarly, the algorithm based on the filtered and normalized cross-correlation histogram was also tested. A similar trend was observed in the value of the confidence of connection but, again, the range obtained from this approach is not clear, opposing to the fixed range between a confidence of connection of -1 and 1 provided by the algorithm proposed herein (**Figure V-11**).

5.4 Stomachs

After validation, the algorithm was tested in engineered neuronal networks *in vitro*. The stomachs structures provide a fixed structural connectivity between neurons that can be extracted from the data recorded from multi-electrode arrays. Each microelectrode array comprised six isolated circuits.

The voltage traces from each electrode were filtered and spikes were detected to obtain the spike train data. Since neurons are placed onto each node, each electrode records activity from more than one cell. This information is important when selecting the appropriate parameters for the spike detection algorithm. Since spikes detected in each electrode can be fired by different neurons, imposing a dead time between spikes in a given electrode might remove spikes that may belong to different units and, thus, relevant data for the dynamics of the circuit may be lost. Therefore, spikes were detected with no dead time imposed.

The algorithm proposed was first used to detect connections without considering individual circuits. The connectivity matrix provides poor information about the spatial patterns of

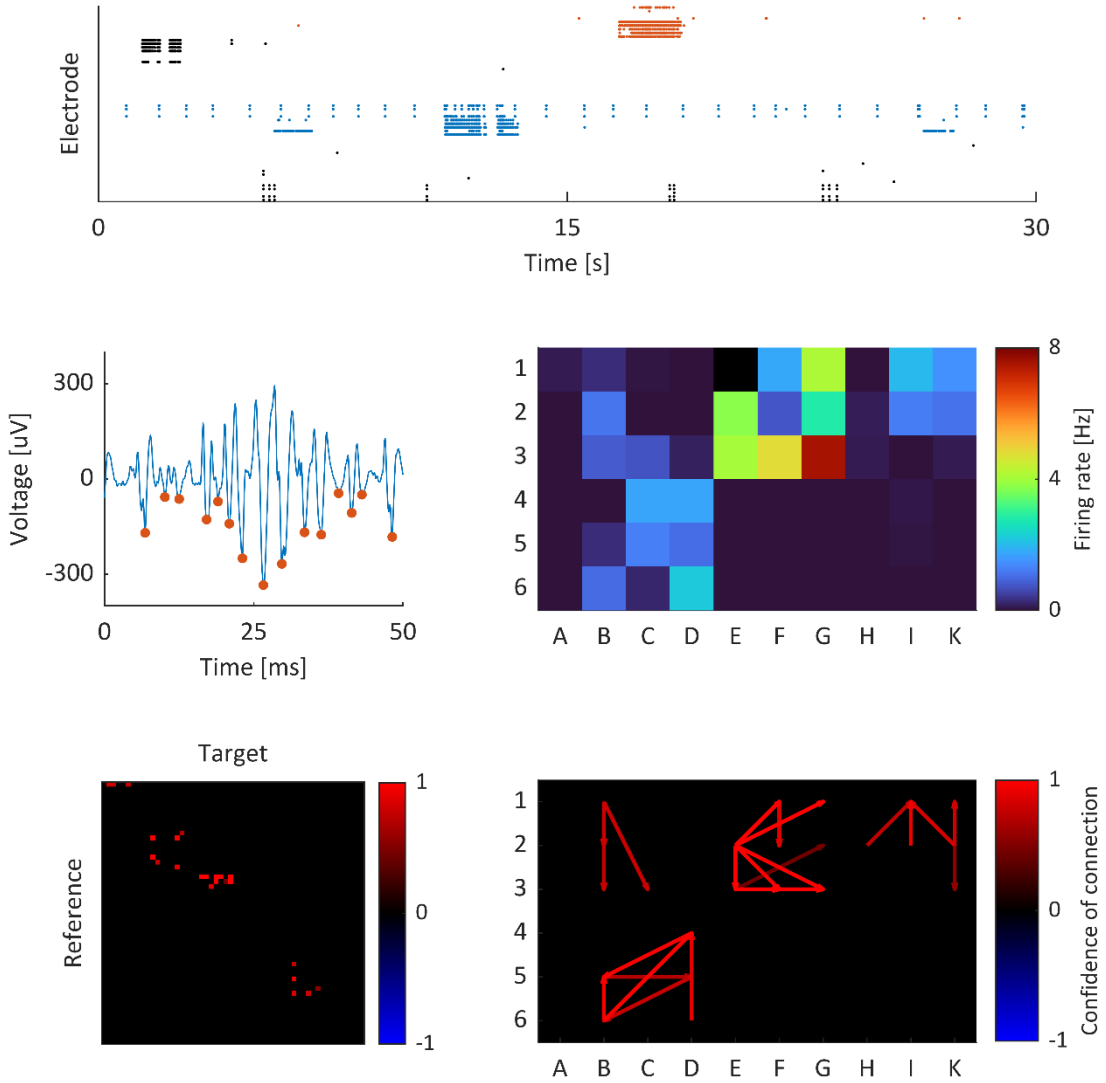

Figure V-12. Connectivity information from the compartmentalized microstructures exhibiting "stomach"-like motifs. In the top panel, the raster plot is shown. The voltage trace for a given electrode is presented, highlighting the detected events. The full activity map is show. Finally, connectivity matrix and the corresponding connectivity map are presented.

connectivity, but looking into the connectivity map allows to conclude that the individual circuits appear isolated, without any connections between them (**Figure V-12**).

Then, a single circuit was evaluated, choosing one that exhibited higher firing rates (**Figure V-13**). The connectivity matrix along with the corresponding delays between firing units, in this case, electrodes, reveal connections with a delay compatible with what is expected between individual electrodes, but also individual neurons [31]. In fact, it is difficult to distinguish between connections that arise from interactions between individual neurons and signals propagating within the same cell, but recorded at different points of the neuron, since axons from neurons seeded on a given node can in escape into the subsequent nodes. Importantly, the direction signal propagation considering the whole circuit seems to reconstruct the unidirectional and anti-

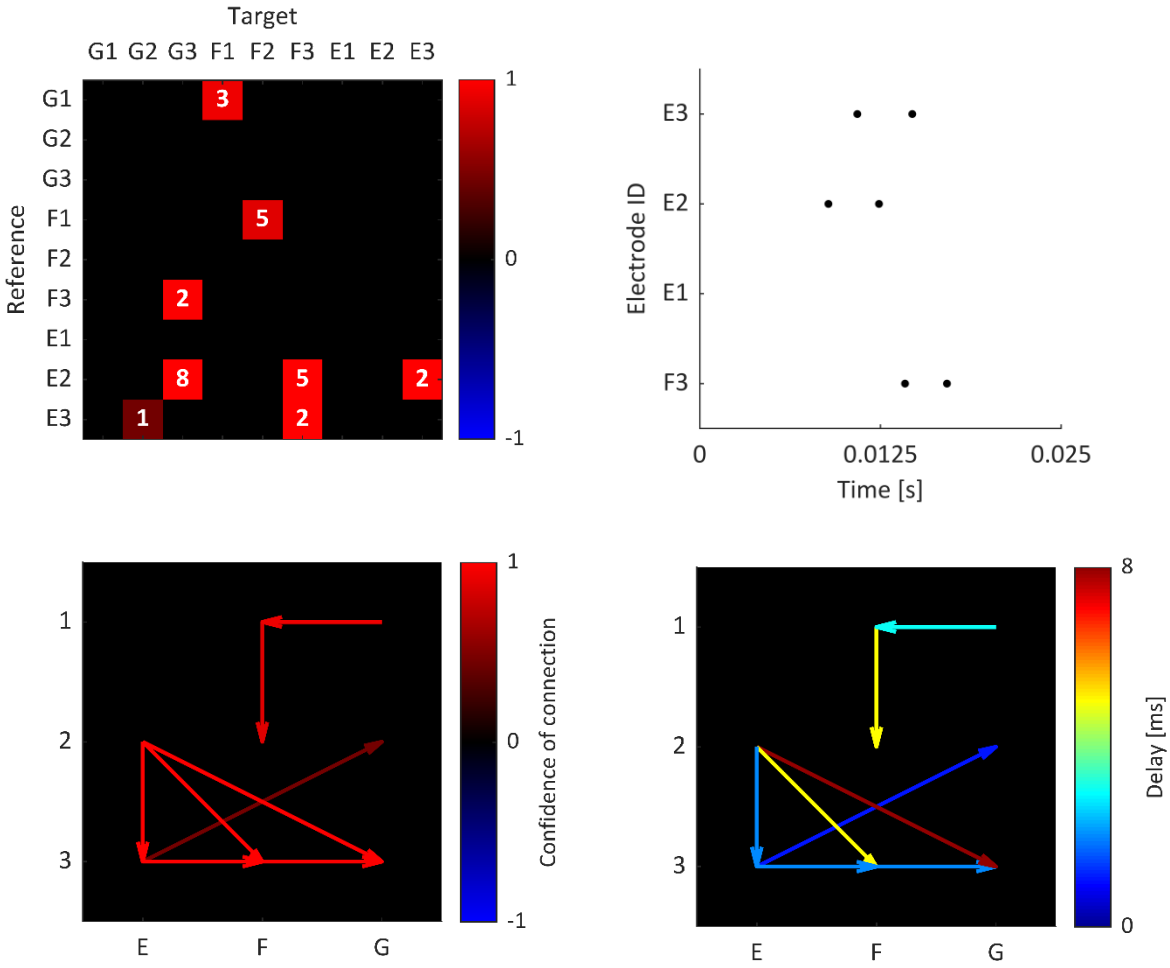

Figure V-13. Connectivity information for a given circuit from the compartmentalized microstructures exhibiting "stomach"-like motifs. In the top left corner, the connectivity matrix, along with the corresponding delays for the detected connections are shown. In the top right corner, the raster plot for four electrodes is shown. Finally, connectivity map and the delay map are presented below.

clockwise direction imposed by the microfluidic compartment. Inhibitory connections were rarely detected, with some circuits not displaying any connection of this type. The balance between excitatory and inhibitory connections in neuronal cultures is approximately 4:1. The lower ratio of inhibitory connections make these connections more difficult to detect. Also, since we are considering events detected in each electrode as a sum of events fired by different units, the total effect between electrodes is, in fact, a sum of putative excitatory and inhibitory interactions, which can hide minor inhibitory effects.

Considering the real-time update of the connectivity matrix for a given connection, real experimental data results in more jagged probability density functions. Therefore, the threshold for the error band was increased to allow a less sensitive analysis of the circuits to noise (n = 5). The convergence of the confidence of connection was highly variable, depending on the firing rate of the cultures.

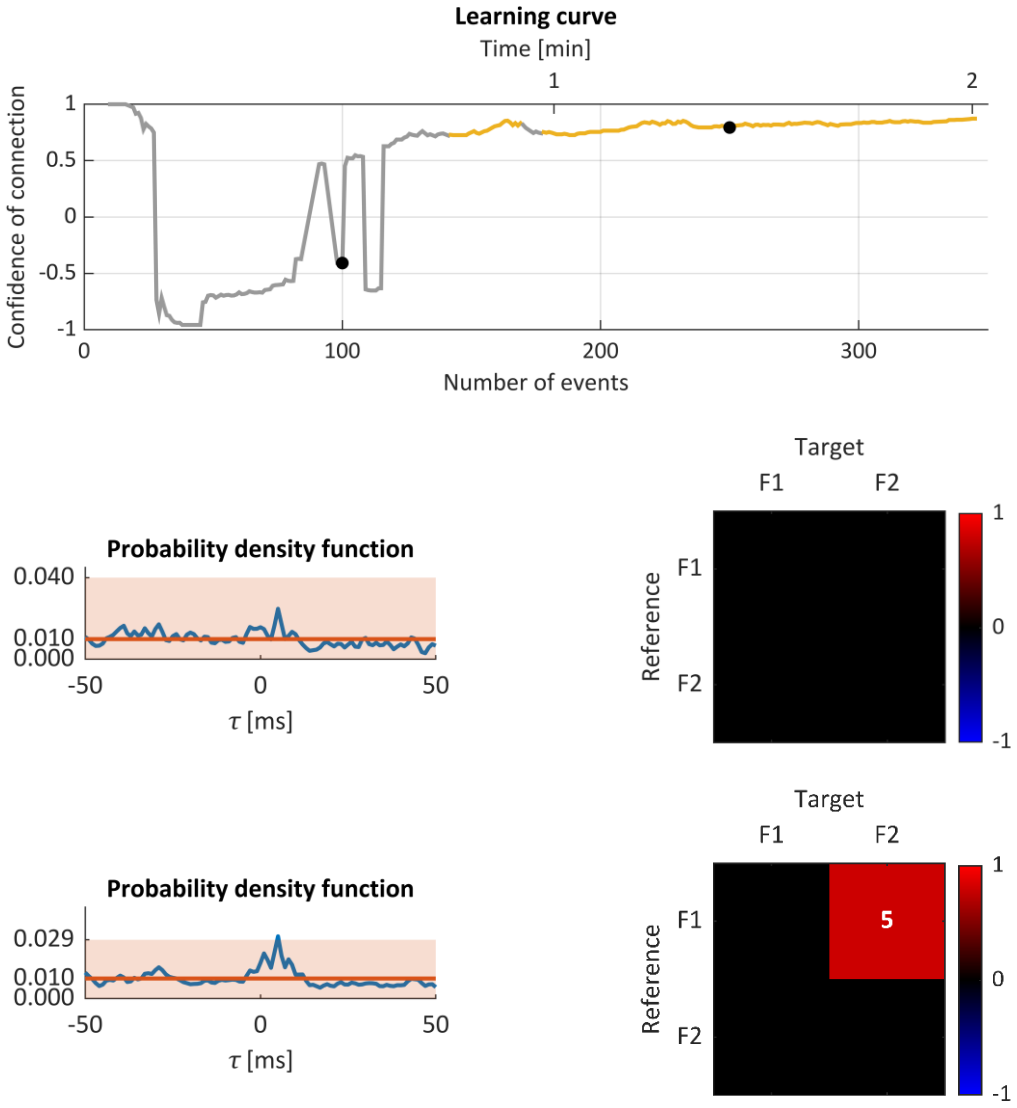

Figure V-14. Learning curve for the evolution of the value of confidence of connection for a given pair of electrodes as a function of the number of detected events. The black markers in the learning curve correspond to the pairs of probability density function and connectivity matrix displayed below.

5.5 Microchannels

Probing neuronal cells that extend their axons through microchannels can provide information about the propagation characteristics of the signal. The algorithm was tested only considering electrodes placed under the microchannels. Bursting periods were removed from the signals since the detection of spikes within these periods is challenging due to the overlap between spikes from different axons that coexist in the same microchannel.

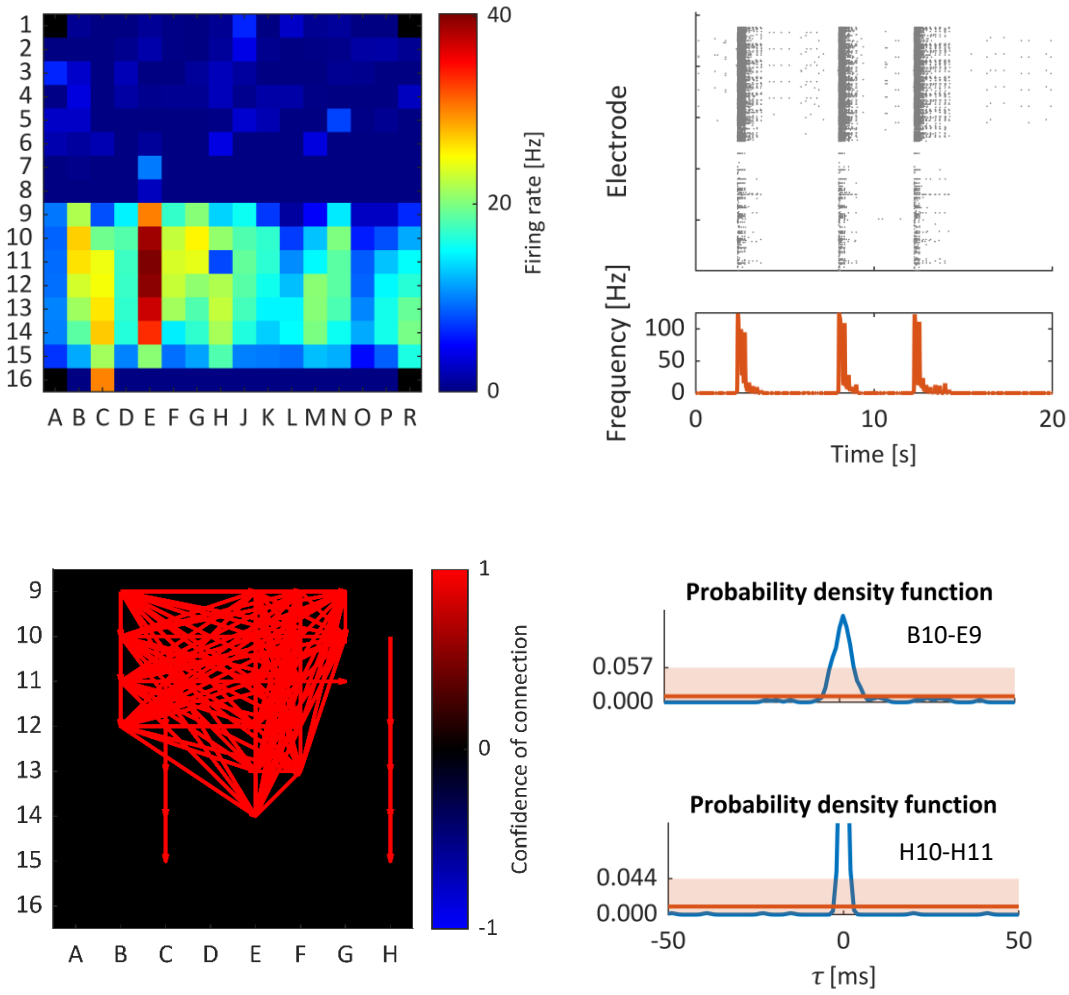

Figure V-15. Connectivity data extracted from compartmentalized microchannel systems. In the top left corner, the full activity map of the microelectrode and microfluidic device is shown, with a significant higher firing rate within the electrodes located below the microchannels. In the top right corner, the raster plot and the corresponding mean instantaneous firing rate of the neuronal culture are presented. The connectivity information extracted from this recording is summarized in the connectivity map presented in the bottom left corner. In the bottom right corner, two examples of estimated probability density function corresponding to electrodes from different and within the same microchannels are presented.

Within a recording time of 10 min, the connectivity map shows propagation down the microchannels, which is compatible with the extending of axon from the somal compartment towards the microchannels. However, other connections between microchannels were also detected. By inspecting the probability density function corresponding to these unexpected connections, significant peaks can indeed be found outside the error band. A possible explanation for this is the fact that we are analysing a data from microchannels whose axons are extending from somas that exist in the somal compartment. Possible synchronization between neurons or

different neurites from the same neuron can result in correlations between electrodes in different microchannels.

5.6 Real-time analysis

Up to this point, all network connectivity analyses have only considered pre-recorded neuronal activity data. To simulate real-time signal acquisition and network inference, single spikes were sequentially provided to the algorithm. This approach is valid as long as the time interval between detected spikes is larger than the computational time required to process each individual spike.

To validate the real-time component of the proposed algorithm, multi-electrode neuronal activity data was acquired in "real-time", with batches of 500 ms per electrode being transmitted to the workstation as they were available. For each batch, the algorithm was executed for each individual spike and the connectivity information updated at each iteration. Again, bursting activity was ignored by estimating the mean instantaneous firing rate of the neuronal population. This was important due to the difficulty to accurately detect spikes within these periods and, as a result, also reduced the computational load that could compromise the detection of relevant interactions in real-time. The average time required to process each detected spike was 3.1±0.1. ms. If more than one spike is detected within this interval, the algorithm will no longer be able to provide estimates in real-time. Therefore, the mean instantaneous frequency rate was limited to 5 Hz. Also, the number of monitored electrodes was limited to 60. When dealing with a single event, the algorithm has to inspect possible connections between the firing unit and all the other possible units. The computational time required for these computations increases with the number of units being considered, in this case, with the number of electrodes. Importantly, such limitations are intrinsically related with the environment where the pipeline is executed. The algorithm was executed in a Windows machine running MATLAB, which is not the ideal environment for high-performance computation, limiting the number of electrodes that can be effectively recorded simultaneously.

Although the low firing rate of *in vitro* neuronal cultures can limit the number of connections that can be detected, the sparsity of the obtained connectivity matrix from an unconstrained culture could be explained by the existence of few neurons that consistently determine the activity of other neurons, or even the whole network, in these conditions. Although structurally densely connected, only a few functional connections highlight from a considerable number of significantly weaker connections (panels **B** and **C** from **Figure V-16**). The evolution of the connectivity matrix with recording time was monitored by computing the accumulated mean square successive differences between consecutive batches. This curve provides a visual representation of how and when the connectivity matrix converges to its final values.

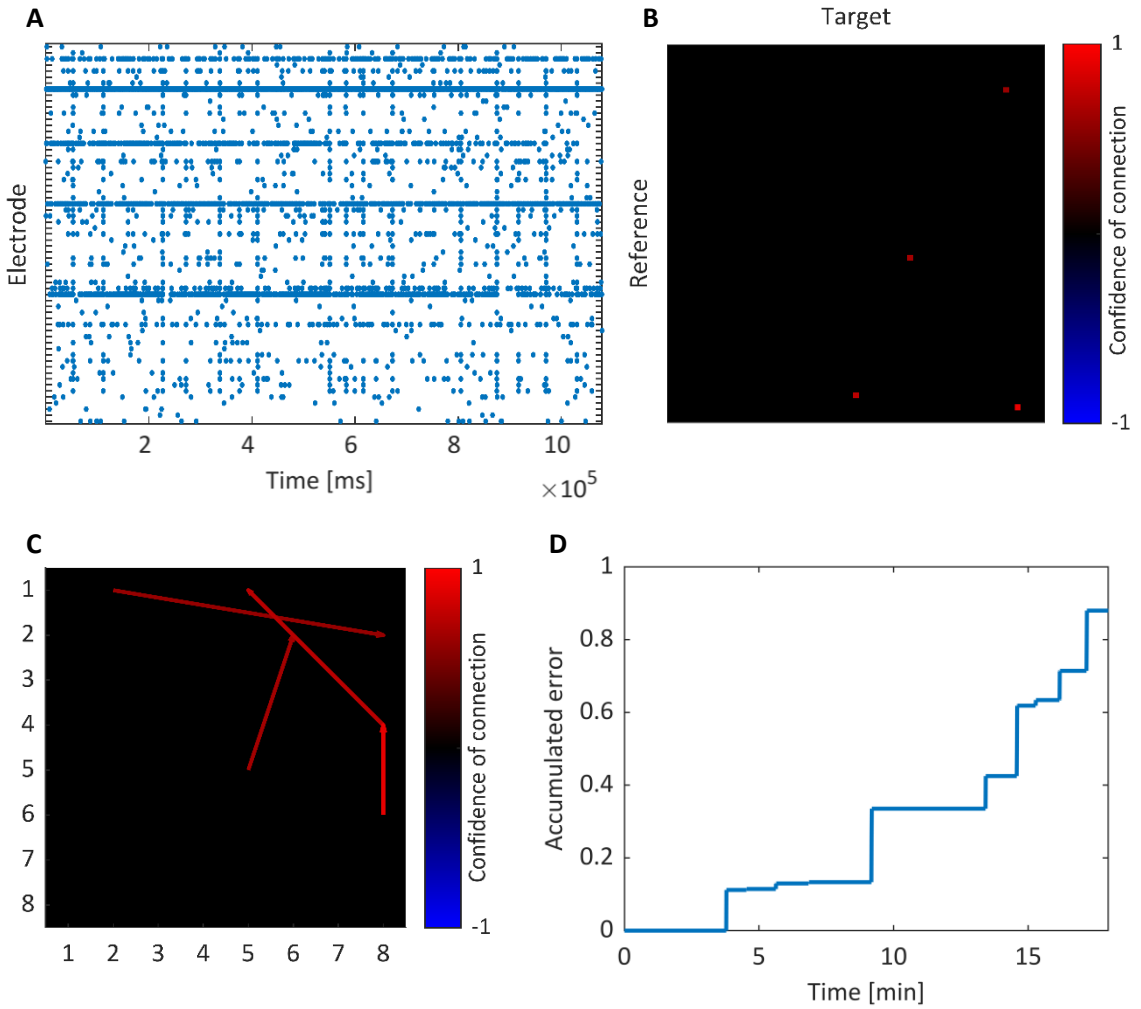

Figure V-16. Network connectivity inference from multi-electrode recordings in "real-time". (A) Raster plot of neuronal activity (spike data) considering all 60 microelectrodes. (B) Final connectivity matrix obtained at the end of the recording. (C) Final connectivity map obtained at the end of the recording. The corresponding delay map is not shown here. (D) Evolution of the accumulated mean square successive differences with recording time. (E) On the left, the estimated probability density function corresponding to pair of electrodes with no significant connection is depicted; on the right, another example corresponding to a pair of electrodes with a significant connection is shown.

Overall, the computational analysis methods were successful in providing estimates of the confidence of connection for both *in silico* and *in vitro* neuronal networks in "real-time". The fact that the algorithm does not have access to the whole recording time as connections are inferred did not limit its potential to detect significant connections above the baseline levels corresponding to spurious or very weak connections with low implications in the dynamics of the neuronal networks. Such connections are usually detected with other approaches, at its removal requires thresholding methods based on the overall network connectivity. Moreover, this approach provides an intuitive and robust measure of confidence of connection within a fixed range, and the characterization of connections in terms of strength, direction and latency, which lacks in other approaches, was also achieved.

Chapter VI

Conclusion

The rich repertoire of spatiotemporal activity patterns exhibited by neuronal assemblies emerges from a complex interplay between the intrinsic properties of individual neurons and their dynamic interactions with other neuronal and non-neuronal cells. Distinct patterns of connectivity among different neuronal types give rise to intricately organized networks that support neurophysiological processes across multiple scales. Extensive alterations in the network connectivity can severely compromise normal neuronal function. In fact, increasing evidence suggests that such connectivity abnormalities are strongly implicated in the pathophysiology of neurological disorders, such as schizophrenia and Alzheimer's disease.

Understanding the complex structure-function relationship in the nervous system, both in healthy and pathological conditions, is a key challenge in modern neuroscience. The comprehensive mapping of neuronal connections in biologically relevant neuronal circuits represents an important step towards bridging this gap. The present work focused on the detection and further characterization of neuronal interactions at the mesoscopic level from *in vitro* electrophysiology recordings. Modern electrophysiological tools provide multi-neuronal activity data at unprecedented temporal and spatial resolutions, thereby revealing functional and/or effective connections down to the single-cell level. A novel correlation-based algorithm was herein proposed for the reconstruction of the detailed wiring diagram of neuronal circuits from spike train data. Significant excitatory and inhibitory connections are detected by quantifying the deviation of the normalized distribution – density histogram – from the expected theoretical distribution for two independently firing units. Information about the confidence of the connection, its latency and direction are extracted from the density histogram, and summarized in informative and intuitive visual representations of neuronal connectivity. The algorithm was successfully validated with synthetic spike train data obtained from computational neuronal simulations for different types of connections. The detection of significant interaction was highly

dependent on the level of activity of the firing units, with higher firing rates providing a faster convergence to the real confidence level of connection. The algorithm was further tested on real experimental data and revealed to be effective at identifying the imposed structure by microfluidic compartmentalization. Going a step further, a real-time implementation of such computational analysis methods was proposed. Connectivity information was successfully extracted from electrophysiological activity in "real-time" for 60-channel microelectrodes.

Even though there are still limitations in this framework, this work provides a set of tools that can be further refined to efficiently deal with increasing number of neurons/electrodes recorded from state-of-the-art high-density probes. Most importantly, these approaches pave the way for connectivity-informed approaches in electrophysiology.

6.1 Future work

The present work proposes a novel computational framework for inferring neuronal connectivity in biological neuronal networks from multi-site electrophysiology recordings in real-time. However, there are still many open challenges and new opportunities for further improvements.

First, concerning the neural recording data from which neuronal connectivity is inferred, single-cell resolution is not feasible using conventional electrophysiology tools. Several neuronal units contribute to the electrical signals recorded by each individual electrode within microelectrode arrays. Therefore, interactions between electrodes may result from multiple synaptic connections between nearby individual neurons, which can potentially hide relevant effects. Automated spike sorting algorithms could be integrated into the data processing pipeline to extract single-neuron activity and, thus, estimate neuronal connections among individual neuronal cells.

Regarding the algorithm developed, cross-correlation metrics are informative and easy to interpret, but they are unable to capture non-linearities and do not allow to distinguish direct and indirect effects between neuronal elements. In some contexts, combining other model-based approaches may be appropriate to reconstruct complex traits of neuronal networks. Moreover, further characterization of network architecture based on graph theory metrics could be interesting addition to the pipeline, providing information on commonly found network elements (*e.g*, hubs) and motifs.

The connectivity inference framework is highly dependent on the level of activity exhibited by the neuronal culture. However, *in vitro* cultures not always present the ideal conditions for inferring neuronal connectivity – high firing rates. Optogenetic and stimulation protocols could be designed to achieve better experimental conditions and reveal the structure of neuronal circuits.

However, this should be done carefully since stimulation can induce neuroplasticity phenomena in neuronal networks and drastically change their dynamics.

Another limiting aspect of this work is the scalability of the computational methods. Since a pairwise comparison between all possible combinations of neurons/electrodes is used to detect putative connections, computational time scales with an increase in the number of neuronal elements. Considering the state-of-the-art technologies featuring high-density recording capabilities, data processing, especially in real-time, would be compromised. In this work, the proposed pipeline was implemented in the MATLAB environment. However, other programming language, such as C/C++, should be considered to enhance the performance of the proposed pipeline.

References

[1] G. M. Shepherd, *Foundations of the Neuron Doctrine: 25th Anniversary Edition*. Oxford University Press, 2015.

[2] R. Yuste, 'From the neuron doctrine to neural networks', *Nat. Rev. Neurosci.*, vol. 16, no. 8, Art. no. 8, Aug. 2015, doi: 10.1038/nrn3962.

[3] V. A. Makarov, F. Panetsos, and O. de Feo, 'A method for determining neural connectivity and inferring the underlying network dynamics using extracellular spike recordings', *J. Neurosci. Methods*, vol. 144, no. 2, pp. 265–279, Jun. 2005, doi: 10.1016/j.jneumeth.2004.11.013.

[4] M. Montalà-Flaquer *et al.*, 'Rich dynamics and functional organization on topographically designed neuronal networks in vitro', *iScience*, vol. 25, no. 12, p. 105680, Dec. 2022, doi: 10.1016/j.isci.2022.105680.

[5] L. E. Suárez, R. D. Markello, R. F. Betzel, and B. Misic, 'Linking Structure and Function in Macroscale Brain Networks', *Trends Cogn. Sci.*, vol. 24, no. 4, pp. 302–315, Apr. 2020, doi: 10.1016/j.tics.2020.01.008.

[6] D. R. Chialvo, 'Emergent complex neural dynamics', *Nat. Phys.*, vol. 6, no. 10, pp. 744–750, Oct. 2010, doi: 10.1038/nphys1803.

[7] M. Rubinov and O. Sporns, 'Complex network measures of brain connectivity: Uses and interpretations', *NeuroImage*, vol. 52, no. 3, pp. 1059–1069, Sep. 2010, doi: 10.1016/j.neuroimage.2009.10.003.

[8] O. Sporns, 'Structure and function of complex brain networks', *Dialogues Clin. Neurosci.*, vol. 15, no. 3, pp. 247–262, Sep. 2013, doi: 10.31887/DCNS.2013.15.3/osporns.

[9] A. Holtmaat and P. Caroni, 'Functional and structural underpinnings of neuronal assembly formation in learning', *Nat. Neurosci.*, vol. 19, no. 12, Art. no. 12, Dec. 2016, doi: 10.1038/nn.4418.

[10] J. S. Damoiseaux, 'Effects of aging on functional and structural brain connectivity', *NeuroImage*, vol. 160, pp. 32–40, Oct. 2017, doi: 10.1016/j.neuroimage.2017.01.077.

[11] M. Pievani, N. Filippini, M. P. van den Heuvel, S. F. Cappa, and G. B. Frisoni, 'Brain connectivity in neurodegenerative diseases—from phenotype to proteinopathy', *Nat. Rev. Neurol.*, vol. 10, no. 11, Art. no. 11, Nov. 2014, doi: 10.1038/nrneurol.2014.178.

[12] 'Dysconnection in Schizophrenia: From Abnormal Synaptic Plasticity to Failures of Self-monitoring | Schizophrenia Bulletin | Oxford Academic'. https://academic.oup.com/schizophreniabulletin/article/35/3/509/1870881 (accessed Aug. 14, 2023).

[13] E. Bullmore and O. Sporns, 'Complex brain networks: graph theoretical analysis of structural and functional systems', *Nat. Rev. Neurosci.*, vol. 10, no. 3, pp. 186–198, Mar. 2009, doi: 10.1038/nrn2575.

[14] O. Sporns, G. Tononi, and R. Kötter, 'The Human Connectome: A Structural Description of the Human Brain', *PLOS Comput. Biol.*, vol. 1, no. 4, p. e42, Sep. 2005, doi: 10.1371/journal.pcbi.0010042.

[15] D. Poli, V. P. Pastore, and P. Massobrio, 'Functional connectivity in in vitro neuronal assemblies', *Front. Neural Circuits*, vol. 9, 2015, Accessed: Feb. 03, 2023. [Online]. Available: https://www.frontiersin.org/articles/10.3389/fncir.2015.00057

[16] A. Horn and M. D. Fox, 'Opportunities of connectomic neuromodulation', *NeuroImage*, vol. 221, p. 117180, Nov. 2020, doi: 10.1016/j.neuroimage.2020.117180.

[17] D. L. de Castro, M. Aroso, A. P. Aguiar, D. B. Grayden, and P. Aguiar, 'A novel closed-loop control algorithm to disrupt pathological neuronal oscillations – implementation and validation in vitro'. bioRxiv, p. 2022.07.05.498735, Jul. 06, 2022. doi: 10.1101/2022.07.05.498735.

[18] M. P. van den Heuvel and O. Sporns, 'Network hubs in the human brain', *Trends Cogn. Sci.*, vol. 17, no. 12, pp. 683–696, Dec. 2013, doi: 10.1016/j.tics.2013.09.012.

[19] P. Bonifazi *et al.*, 'GABAergic Hub Neurons Orchestrate Synchrony in Developing Hippocampal Networks', *Science*, vol. 326, pp. 1419–24, Dec. 2009, doi: 10.1126/science.1175509.

[20] J. Jimenez-Shahed, 'Device profile of the percept PC deep brain stimulation system for the treatment of Parkinson's disease and related disorders', *Expert Rev. Med. Devices*, vol. 18, no. 4, pp. 319–332, Apr. 2021, doi: 10.1080/17434440.2021.1909471.
[21] M. L. Kringelbach, N. Jenkinson, S. L. F. Owen, and T. Z. Aziz, 'Translational principles of deep brain stimulation', *Nat. Rev. Neurosci.*, vol. 8, no. 8, Art. no. 8, Aug. 2007, doi: 10.1038/nrn2196.
[22] S. Chiken and A. Nambu, 'Mechanism of Deep Brain Stimulation: Inhibition, Excitation, or Disruption?', *The Neuroscientist*, vol. 22, no. 3, pp. 313–322, Jun. 2016, doi: 10.1177/1073858415581986.
[23] A. M. Oliveira, L. Coelho, E. Carvalho, M. J. Ferreira-Pinto, R. Vaz, and P. Aguiar, 'Machine learning for adaptive deep brain stimulation in Parkinson's disease: closing the loop', *J. Neurol.*, Aug. 2023, doi: 10.1007/s00415-023-11873-1.
[24] I. Magrans de Abril, J. Yoshimoto, and K. Doya, 'Connectivity inference from neural recording data: Challenges, mathematical bases and research directions', *Neural Netw.*, vol. 102, pp. 120–137, Jun. 2018, doi: 10.1016/j.neunet.2018.02.016.
[25] M. Glickstein, 'Golgi and Cajal: The neuron doctrine and the 100th anniversary of the 1906 Nobel Prize', vol. 16, no. 5.
[26] M. R. Muzio and M. Cascella, 'Histology, Axon', in *StatPearls*, Treasure Island (FL): StatPearls Publishing, 2023. Accessed: Jun. 19, 2023. [Online]. Available: http://www.ncbi.nlm.nih.gov/books/NBK554388/
[27] J. S. Kim and M. Zhen, 'Neuronal Polarity', in *Encyclopedia of Neuroscience*, M. D. Binder, N. Hirokawa, and U. Windhorst, Eds., Berlin, Heidelberg: Springer, 2009, pp. 2789–2792. doi: 10.1007/978-3-540-29678-2_3921.
[28] 'Cellular diversity in the hippocampus | Janelia Research Campus'. https://www.janelia.org/lab/spruston-lab/research/cellular-diversity-in-the-hippocampus (accessed Aug. 15, 2023).
[29] H. Zeng and J. R. Sanes, 'Neuronal cell-type classification: challenges, opportunities and the path forward', *Nat. Rev. Neurosci.*, vol. 18, no. 9, Art. no. 9, Sep. 2017, doi: 10.1038/nrn.2017.85.
[30] S. A. Booker and I. Vida, 'Morphological diversity and connectivity of hippocampal interneurons', *Cell Tissue Res.*, vol. 373, no. 3, pp. 619–641, Sep. 2018, doi: 10.1007/s00441-018-2882-2.
[31] 'Physiology, Synapse - StatPearls - NCBI Bookshelf'. https://www.ncbi.nlm.nih.gov/books/NBK526047/ (accessed Jul. 12, 2023).
[32] P. Caroni, F. Donato, and D. Muller, 'Structural plasticity upon learning: regulation and functions', *Nat. Rev. Neurosci.*, vol. 13, no. 7, Art. no. 7, Jul. 2012, doi: 10.1038/nrn3258.
[33] 'Glia — more than just brain glue | Nature'. https://www.nature.com/articles/457675a (accessed Jul. 12, 2023).
[34] I. Chen and F. Lui, 'Neuroanatomy, Neuron Action Potential', in *StatPearls*, Treasure Island (FL): StatPearls Publishing, 2023. Accessed: Jul. 12, 2023. [Online]. Available: http://www.ncbi.nlm.nih.gov/books/NBK546639/
[35] B. Alberts, A. Johnson, J. Lewis, M. Raff, K. Roberts, and P. Walter, 'Ion Channels and the Electrical Properties of Membranes', in *Molecular Biology of the Cell. 4th edition*, Garland Science, 2002. Accessed: Jul. 12, 2023. [Online]. Available: https://www.ncbi.nlm.nih.gov/books/NBK26910/
[36] D. C. Sterratt, B. P. Graham, A. J. Gillies, and D. J. Willshaw, 'Principles of Neuronal Modelling OR Principles of Computational Neuroscience OR Computational Modelling in Neuroscience'.
[37] A. L. Hodgkin, A. F. Huxley, and B. Katz, 'Measurement of current-voltage relations in the membrane of the giant axon of Loligo', *J. Physiol.*, vol. 116, no. 4, pp. 424–448, Apr. 1952.
[38] M. E. J. Obien, K. Deligkaris, T. Bullmann, D. J. Bakkum, and U. Frey, 'Revealing neuronal function through microelectrode array recordings', *Front. Neurosci.*, vol. 8, 2015, Accessed: Mar. 13, 2023. [Online]. Available: https://www.frontiersin.org/articles/10.3389/fnins.2014.00423

[39] J. Gao, C. Liao, S. Liu, T. Xia, and G. Jiang, 'Nanotechnology: new opportunities for the development of patch-clamps', *J. Nanobiotechnology*, vol. 19, no. 1, p. 97, Apr. 2021, doi: 10.1186/s12951-021-00841-4.

[40] 'Heart on a Chip — Extracellular Multielectrode Recordings from Cardiac Myocytes in Vitro | SpringerLink'. https://link.springer.com/chapter/10.1007/3-540-26574-0_22 (accessed Sep. 19, 2023).

[41] J. Duru *et al.*, 'Engineered Biological Neural Networks on High Density CMOS Microelectrode Arrays', *Front. Neurosci.*, vol. 16, 2022, Accessed: Jul. 10, 2023. [Online]. Available: https://www.frontiersin.org/articles/10.3389/fnins.2022.829884

[42] J. Müller *et al.*, 'High-resolution CMOS MEA platform to study neurons at subcellular, cellular, and network levels', *Lab. Chip*, vol. 15, no. 13, pp. 2767–2780, 2015, doi: 10.1039/C5LC00133A.

[43] N. A. Steinmetz *et al.*, 'Neuropixels 2.0: A miniaturized high-density probe for stable, long-term brain recordings', *Science*, vol. 372, no. 6539, p. eabf4588, Apr. 2021, doi: 10.1126/science.abf4588.

[44] I. H. Stevenson and K. P. Kording, 'How advances in neural recording affect data analysis', *Nat. Neurosci.*, vol. 14, no. 2, Art. no. 2, Feb. 2011, doi: 10.1038/nn.2731.

[45] A. P. Buccino, S. Garcia, and P. Yger, 'Spike sorting: new trends and challenges of the era of high-density probes', *Prog. Biomed. Eng.*, vol. 4, no. 2, p. 022005, May 2022, doi: 10.1088/2516-1091/ac6b96.

[46] C. Grienberger and A. Konnerth, 'Imaging Calcium in Neurons', *Neuron*, vol. 73, no. 5, pp. 862–885, Mar. 2012, doi: 10.1016/j.neuron.2012.02.011.

[47] H. Kennedy, D. C. Van Essen, and Y. Christen, Eds., *Micro-, Meso- and Macro-Connectomics of the Brain*. in Research and Perspectives in Neurosciences. Cham: Springer International Publishing, 2016. doi: 10.1007/978-3-319-27777-6.

[48] D. Jäckel *et al.*, 'Combination of High-density Microelectrode Array and Patch Clamp Recordings to Enable Studies of Multisynaptic Integration', *Sci. Rep.*, vol. 7, no. 1, Art. no. 1, Apr. 2017, doi: 10.1038/s41598-017-00981-4.

[49] S. Song, P. J. Sjöström, M. Reigl, S. Nelson, and D. B. Chklovskii, 'Highly Nonrandom Features of Synaptic Connectivity in Local Cortical Circuits', *PLOS Biol.*, vol. 3, no. 3, p. e68, Mar. 2005, doi: 10.1371/journal.pbio.0030068.

[50] L. Campagnola *et al.*, 'Local connectivity and synaptic dynamics in mouse and human neocortex', *Science*, vol. 375, no. 6585, p. eabj5861, Mar. 2022, doi: 10.1126/science.abj5861.

[51] R. F. Betzel, L. Byrge, Y. He, J. Goñi, X.-N. Zuo, and O. Sporns, 'Changes in structural and functional connectivity among resting-state networks across the human lifespan', *NeuroImage*, vol. 102, pp. 345–357, Nov. 2014, doi: 10.1016/j.neuroimage.2014.07.067.

[52] R. L. Buckner, F. M. Krienen, and B. T. T. Yeo, 'Opportunities and limitations of intrinsic functional connectivity MRI', *Nat. Neurosci.*, vol. 16, no. 7, Art. no. 7, Jul. 2013, doi: 10.1038/nn.3423.

[53] F. Zamani Esfahlani, J. Faskowitz, J. Slack, B. Mišić, and R. F. Betzel, 'Local structure-function relationships in human brain networks across the lifespan', *Nat. Commun.*, vol. 13, no. 1, Art. no. 1, Apr. 2022, doi: 10.1038/s41467-022-29770-y.

[54] M. Butz, F. Wörgötter, and A. van Ooyen, 'Activity-dependent structural plasticity', *Brain Res. Rev.*, vol. 60, no. 2, pp. 287–305, May 2009, doi: 10.1016/j.brainresrev.2008.12.023.

[55] J. G. White, E. Southgate, J. N. Thomson, and S. Brenner, 'The Structure of the Nervous System of the Nematode Caenorhabditis elegans', *Philos. Trans. R. Soc. Lond. B. Biol. Sci.*, vol. 314, no. 1165, pp. 1–340, 1986.

[56] C. M. Hales, J. D. Rolston, and S. M. Potter, 'How to culture, record and stimulate neuronal networks on micro-electrode arrays (MEAs)', *J. Vis. Exp. JoVE*, no. 39, p. 2056, May 2010, doi: 10.3791/2056.

[57] P. Bonifazi and P. Massobrio, 'Reconstruction of Functional Connectivity from Multielectrode Recordings and Calcium Imaging', in *In Vitro Neuronal Networks*, M. Chiappalone, V. Pasquale, and M. Frega, Eds., in Advances in Neurobiology, vol. 22. Cham: Springer International Publishing, 2019, pp. 207–231. doi: 10.1007/978-3-030-11135-9_9.

[58] ‘Model-Free Reconstruction of Excitatory Neuronal Connectivity from Calcium Imaging Signals | PLOS Computational Biology’. https://journals.plos.org/ploscompbiol/article?id=10.1371/journal.pcbi.1002653 (accessed Jul. 04, 2023).

[59] C. J. Honey *et al.*, ‘Predicting human resting-state functional connectivity from structural connectivity’, *Proc. Natl. Acad. Sci.*, vol. 106, no. 6, pp. 2035–2040, Feb. 2009, doi: 10.1073/pnas.0811168106.

[60] Y. Osmanlıoğlu *et al.*, ‘System-level matching of structural and functional connectomes in the human brain’, *NeuroImage*, vol. 199, pp. 93–104, Oct. 2019, doi: 10.1016/j.neuroimage.2019.05.064.

[61] K. J. Friston, ‘Functional and Effective Connectivity: A Review’, *Brain Connect.*, vol. 1, no. 1, pp. 13–36, Jan. 2011, doi: 10.1089/brain.2011.0008.

[62] V. Emmenegger, M. E. J. Obien, F. Franke, and A. Hierlemann, ‘Technologies to Study Action Potential Propagation With a Focus on HD-MEAs’, *Front. Cell. Neurosci.*, vol. 13, 2019, Accessed: Jun. 08, 2023. [Online]. Available: https://www.frontiersin.org/articles/10.3389/fncel.2019.00159

[63] T. Nieus, D. Borgonovo, S. Diwakar, G. Aletti, and G. Naldi, ‘A multi-class logistic regression algorithm to reliably infer network connectivity from cell membrane potentials’, *Front. Appl. Math. Stat.*, vol. 8, 2022, Accessed: Feb. 11, 2023. [Online]. Available: https://www.frontiersin.org/articles/10.3389/fams.2022.1023310

[64] M. Ramezanian-Panahi, G. Abrevaya, J.-C. Gagnon-Audet, V. Voleti, I. Rish, and G. Dumas, ‘Generative Models of Brain Dynamics’, *Front. Artif. Intell.*, vol. 5, 2022, Accessed: Jul. 04, 2023. [Online]. Available: https://www.frontiersin.org/articles/10.3389/frai.2022.807406

[65] A. Boschi, M. Brofiga, and P. Massobrio, ‘Thresholding Functional Connectivity Matrices to Recover the Topological Properties of Large-Scale Neuronal Networks’, *Front. Neurosci.*, vol. 15, 2021, Accessed: Feb. 06, 2023. [Online]. Available: https://www.frontiersin.org/articles/10.3389/fnins.2021.705103

[66] V. P. Pastore, P. Massobrio, A. Godjoski, and S. Martinoia, ‘Identification of excitatory-inhibitory links and network topology in large-scale neuronal assemblies from multi-electrode recordings’, *PLOS Comput. Biol.*, vol. 14, no. 8, p. e1006381, Aug. 2018, doi: 10.1371/journal.pcbi.1006381.

[67] M. Garofalo, T. Nieus, P. Massobrio, and S. Martinoia, ‘Evaluation of the Performance of Information Theory-Based Methods and Cross-Correlation to Estimate the Functional Connectivity in Cortical Networks’, *PLOS ONE*, vol. 4, no. 8, p. e6482, Aug. 2009, doi: 10.1371/journal.pone.0006482.

[68] M. R. Cohen and A. Kohn, ‘Measuring and interpreting neuronal correlations’, *Nat. Neurosci.*, vol. 14, no. 7, Art. no. 7, Jul. 2011, doi: 10.1038/nn.2842.

[69] S. B. Hofer *et al.*, ‘Differential connectivity and response dynamics of excitatory and inhibitory neurons in visual cortex’, *Nat. Neurosci.*, vol. 14, no. 8, Art. no. 8, Aug. 2011, doi: 10.1038/nn.2876.

[70] M. Lamberti, M. Hess, I. Dias, M. van Putten, J. le Feber, and S. Marzen, ‘Maximum entropy models provide functional connectivity estimates in neural networks’, *Sci. Rep.*, vol. 12, no. 1, Art. no. 1, Jun. 2022, doi: 10.1038/s41598-022-13674-4.

[71] D. Poli, V. P. Pastore, S. Martinoia, and P. Massobrio, ‘From functional to structural connectivity using partial correlation in neuronal assemblies’, *J. Neural Eng.*, vol. 13, no. 2, p. 026023, Feb. 2016, doi: 10.1088/1741-2560/13/2/026023.

[72] S. Ito, M. E. Hansen, R. Heiland, A. Lumsdaine, A. M. Litke, and J. M. Beggs, ‘Extending Transfer Entropy Improves Identification of Effective Connectivity in a Spiking Cortical Network Model’, *PLOS ONE*, vol. 6, no. 11, p. e27431, Nov. 2011, doi: 10.1371/journal.pone.0027431.

[73] N. Lama, A. Hargreaves, B. Stevens, and T. M. McGinnity, ‘Transfer Entropy Based Connectivity Estimation of Spontaneously Firing Hippocampal Cultures on Multi Electrode Arrays’, in *2019 International Joint Conference on Neural Networks (IJCNN)*, Jul. 2019, pp. 1–8. doi: 10.1109/IJCNN.2019.8851864.

[74] O. Sporns, ‘Graph theory methods: applications in brain networks’, *Dialogues Clin. Neurosci.*, vol. 20, no. 2, pp. 111–121, Jun. 2018.
[75] D. Lonardoni, H. Amin, S. D. Marco, A. Maccione, L. Berdondini, and T. Nieus, ‘Recurrently connected and localized neuronal communities initiate coordinated spontaneous activity in neuronal networks’, *PLOS Comput. Biol.*, vol. 13, no. 7, p. e1005672, Jul. 2017, doi: 10.1371/journal.pcbi.1005672.
[76] S. De Blasi, M. Ciba, A. Bahmer, and C. Thielemann, ‘Total spiking probability edges: A cross-correlation based method for effective connectivity estimation of cortical spiking neurons’, *J. Neurosci. Methods*, vol. 312, pp. 169–181, Jan. 2019, doi: 10.1016/j.jneumeth.2018.11.013.
[77] P. D. Heeger, ‘Poisson Model of Spike Generation’.
[78] M. L. Hines and N. T. Carnevale, ‘The NEURON simulation environment’, *Neural Comput.*, vol. 9, no. 6, pp. 1179–1209, Aug. 1997, doi: 10.1162/neco.1997.9.6.1179.
[79] ‘NEURON | empirically-based simulations of neurons and networks of neurons’. https://www.neuron.yale.edu/neuron/ (accessed Jul. 17, 2023).
[80] ‘ModelDB: Home’. https://senselab.med.yale.edu/ModelDB/ (accessed Jul. 18, 2023).
[81] ‘Expanding NEURON’s repertoire of mechanisms with NMODL - PubMed’. https://pubmed.ncbi.nlm.nih.gov/10905805/ (accessed Jul. 22, 2023).
[82] ‘Artificial Cells in NEURON — NEURON documentation’. https://nrn.readthedocs.io/en/latest/courses/artificial_cells_neuron.html (accessed Jul. 22, 2023).
[83] D. Purves *et al.*, ‘Excitatory and Inhibitory Postsynaptic Potentials’, in *Neuroscience. 2nd edition*, Sinauer Associates, 2001. Accessed: Jul. 18, 2023. [Online]. Available: https://www.ncbi.nlm.nih.gov/books/NBK11117/
[84] G. Stuart, N. Spruston, and M. Häusser, *Dendrites*. Oxford University Press, 2007.
[85] R. Matsumura, H. Yamamoto, T. Hayakawa, S. Katsurabayashi, M. Niwano, and A. Hirano-Iwata, ‘Dependence and Homeostasis of Membrane Impedance on Cell Morphology in Cultured Hippocampal Neurons’, *Sci. Rep.*, vol. 8, no. 1, Art. no. 1, Jul. 2018, doi: 10.1038/s41598-018-28232-0.
[86] P. Aguiar, M. Sousa, and D. Lima, ‘NMDA Channels Together With L-Type Calcium Currents and Calcium-Activated Nonspecific Cationic Currents Are Sufficient to Generate Windup in WDR Neurons’, *J. Neurophysiol.*, vol. 104, no. 2, pp. 1155–1166, Aug. 2010, doi: 10.1152/jn.00834.2009.
[87] R. D. Traub and R. Miles, *Neuronal Networks of the Hippocampus*. Cambridge University Press, 1991.
[88] N. Spruston, G. Stuart, M. Häusser, G. Stuart, N. Spruston, and M. Häusser, Eds., ‘Principles of dendritic integration’, in *Dendrites*, Oxford University Press, 2016, p. 0. doi: 10.1093/acprof:oso/9780198745273.003.0012.
[89] D. Johnston, J. C. Magee, C. M. Colbert, and B. R. Christie, ‘Active Properties of Neuronal Dendrites’, *Annu. Rev. Neurosci.*, vol. 19, no. 1, pp. 165–186, 1996, doi: 10.1146/annurev.ne.19.030196.001121.
[90] ‘3.1 Synapses | Neuronal Dynamics online book’. https://neuronaldynamics.epfl.ch/online/Ch3.S1.html (accessed Jul. 22, 2023).
[91] A. Destexhe and D. Paré, ‘Impact of Network Activity on the Integrative Properties of Neocortical Pyramidal Neurons In Vivo’, *J. Neurophysiol.*, vol. 81, no. 4, pp. 1531–1547, Apr. 1999, doi: 10.1152/jn.1999.81.4.1531.
[92] E. Neto *et al.*, ‘Compartmentalized Microfluidic Platforms: The Unrivaled Breakthrough of *In Vitro* Tools for Neurobiological Research’, *J. Neurosci.*, vol. 36, no. 46, pp. 11573–11584, Nov. 2016, doi: 10.1523/JNEUROSCI.1748-16.2016.
[93] C. Forró *et al.*, ‘Modular microstructure design to build neuronal networks of defined functional connectivity’, *Biosens. Bioelectron.*, vol. 122, pp. 75–87, Dec. 2018, doi: 10.1016/j.bios.2018.08.075.
[94] J. C. Mateus *et al.*, ‘Bidirectional flow of action potentials in axons drives activity dynamics in neuronal cultures’, *J. Neural Eng.*, vol. 18, no. 6, p. 066045, Dec. 2021, doi: 10.1088/1741-2552/ac41db.

[95] I. Miranda *et al.*, 'Properties and Applications of PDMS for Biomedical Engineering: A Review', *J. Funct. Biomater.*, vol. 13, no. 1, p. 2, Dec. 2021, doi: 10.3390/jfb13010002.

[96] R. Q. Quiroga, Z. Nadasdy, and Y. Ben-Shaul, 'Unsupervised Spike Detection and Sorting with Wavelets and Superparamagnetic Clustering', *Neural Comput.*, vol. 16, no. 8, pp. 1661–1687, Aug. 2004, doi: 10.1162/089976604774201631.

[97] A. Maccione, M. Gandolfo, P. Massobrio, A. Novellino, S. Martinoia, and M. Chiappalone, 'A novel algorithm for precise identification of spikes in extracellularly recorded neuronal signals', *J. Neurosci. Methods*, vol. 177, no. 1, pp. 241–249, Feb. 2009, doi: 10.1016/j.jneumeth.2008.09.026.

[98] C. Leys, C. Ley, O. Klein, P. Bernard, and L. Licata, 'Detecting outliers: Do not use standard deviation around the mean, use absolute deviation around the median', *J. Exp. Soc. Psychol.*, vol. 49, no. 4, pp. 764–766, Jul. 2013, doi: 10.1016/j.jesp.2013.03.013.

[99] 'Brain Basics: The Life and Death of a Neuron', *National Institute of Neurological Disorders and Stroke*. https://www.ninds.nih.gov/health-information/public-education/brain-basics/brain-basics-life-and-death-neuron (accessed Jun. 18, 2023).

[100] T. Kispersky, G. J. Gutierrez, and E. Marder, 'Functional connectivity in a rhythmic inhibitory circuit using Granger causality', *Neural Syst. Circuits*, vol. 1, no. 1, p. 9, May 2011, doi: 10.1186/2042-1001-1-9.

[101] 'Pre 1.3 Histogram and probability density function', *TU Delft OCW*. https://ocw.tudelft.nl/course-readings/pre-1-3-histogram-probability-density-function/ (accessed Aug. 10, 2023).

[102] F. M. Dekking, C. Kraaikamp, H. P. Lopuhaä, and L. E. Meester, 'The law of large numbers', in *A Modern Introduction to Probability and Statistics: Understanding Why and How*, F. M. Dekking, C. Kraaikamp, H. P. Lopuhaä, and L. E. Meester, Eds., in Springer Texts in Statistics. London: Springer, 2005, pp. 181–194. doi: 10.1007/1-84628-168-7_13.